Research of Computer-Generated Phase-Only Holograms Based on Gradient-Descent Algorithm

Shujian Liu

Contents

Abstract

The hologram technology is a method to record the amplitude and the phase of the light, which first developed by Dennis Gabor. The invention of the SLM enables processing the hologram through the electric method. The adoption of the phase-only SLM brings the concept of the phase-only computer-generated holograms (phase-only CGH). There is a conventional method to generate the phase-only CGH of 2D images. However, the noise of the holograms is significant. The gradient descent method, also called steepest descent method, is widely utilized in the field of deep learning, is able to be ported to the task of phase-only CGH task. In this research, a gradient-descent method based algorithm is proposed to generate phase-only CGHs of 2D images as a part of the research.

The holograms are famous on 3D regeneration with the utilization of the holographic film, however, the conventional phase-only algorithm based on Fourier transform can only generate the phase-only CGH of 2D images. A Fresnel transform with the utilization of Fresnel lens is proposed to generate holograms of 3D images and reconstruct the images from the holograms. This research also developed an algorithm based on proposed transform and gradient-descent method as a part of the research.

In the field of gradient descent, there are many algorithms based on gradient-descent method, which overall named as gradient descent algorithms, are proved as high efficient algorithms in the task of deep learning. These optimization schemes may also speed up the optimization in the task of phase-only CGH. This research port 6 optimization schemes of gradient-descent method and made a comparison of these optical schemes as a part of the research.

The Fresnel transform with the utilization of Fresnel lens is a general form of Fourier transform in math. This may bring new features to the existing algorithm in many fields which rely on the Fourier transform. In the imaging processing, image encryption, image compression, and blind watermarking is strongly rely on the Fourier transform. In this research, the replacement of Fourier transform with the proposed transform may bring more features to the algorithm as a part of the research.

1 Introduction

1.1 Hologram

Hologram, first invented by Dennis Gabor [1, 2] is a technique that record the amplitude and phase of the wavefront through interfering with a reference beam. By recording the interference pattern with a film, the wavefront is recorded and can be reconstructed through light on the film with the same reference beam by diffraction on the holographic film. Dennis Gabor was awarded a Nobel Prize in physics[3] in 1971 for this invention.

Holograms are widely applicated in art, data storage, sensors, security, lithographym, etc.. Salvador Dalí first employ the holography artistically. Margaret Benyon, In Great Britain, used holograph as medium and held a solo exhibition at 1969[4]. In 2005, Hideyoshi Horimai produced a 120mm disc that uses a holographic layer for data storage with a vast patential up to 3.9TB, which named as Holographic Versatile Disc (HVD)[5, 6, 7, 8]. Holography are also applicated in sensors for glucose sensoring[9], pH sensoring[10], etc.. In the application of security, holographic anti-counterfeiting film[11, 12] and applications on banknote[13, 14] are widely adopted. Holography is also utilized in lithography[15, 16] by generating a hologram to reconstruct the target texture.

A modern optical element created by holographic film, Holographic Optical Element (HOE), are designed to make special optical affect, which is hard to practice in conventional lenses. HOEs are adopted in Augmented Reality devices in modern design[17]. A special kind of HOE, the Digital Designed Holographic Optical Element (DDHOE), are utilized to practice the see-through head up displays[18, 19].

1.2 Computer-Benerated Holograms

With the invention and application of Spatial Light Modulator (SLM), which is able to modulate the phase, amplitude, or polarization of a beam, wave front of the beam can be modulized by computer. A new concept, Computer-Generated Holograms (CGH), appears to generate the holograms through calculation by computer. SLMs are divided into many kinds based on the classification of function. Phase-only SLM and amplitude-only SLM are most common SLMs in optical researchs.

By replacing the Holographic films by SLMs, the wave front can be modulated

by computer. Calculating the hologram by computers become possible. CGHs is the way to generate the hologram on computer. Adapting different SLMs, CGH algorithms varies each other. In this research, I focus on the phase-only holograms with the utilization of a phase-only SLM.

Based on the difference of Fraunhofer Approximation or Fresnel Approximation, the base transform of CGH and virtual optical system differ from each other.

1.2.1 Computer-generated Holograms by Fraunhofer diffraction

Fraunhofer diffraction, or far field diffraction, indicates the status that the plane of observation is located far enough from the aperture. By a utilization of a Fourier transform lens, the observation plane can receive the same result in the Fourier plane (focal plane). The result on the observation is equivalent as Fourier transform of the aperture.

CGH in Fourier field, the hologram of 2D image can be produced and the reconstructed image is located on the Fourier plane. This make the optical system small and is able to design portable devices in practice. CGH in Fourier field is not able to reconstruct a 3D image, because the depth can not be modulated during the Fourier transform.

In the CGH of Fourier field, there is a conventional algorithm, Gerchberg-Saxton (GS) algorithm[20], aiming at phase retrieval, are widely used to generate phase-only holograms[21]. Some algorithms did more optimization based on GS algorithm[22, 23] shows a higher precision and effect. Other algorithms such as as simulated annealing [24], genetic algorithms [25, 26, 27], and direct binary searches [28, 29, 30], have been developed to optimize phase-only CGHs. I proposed an algorithm based on Gradient Descent method succeeded in generating holograms in a revolutional high effect than GS algorithm[31].

1.2.2 Computer-generated Holograms by Fresnel diffraction

Fresnel diffraction, or near field diffraction, indicated the status that the plane of observation is located in the near field of the aperture. The reconstructed image present at the plane of observation directly.

CGH in Fresnel field, the hologram of 3D image can be produced and the reconstructed image is located at the near field of the hologram. However, according to

the precision of the SLM at present, the near field is too long in practice. This made the Fresnel field CGH cannot be directly adopted in portable devices.

In the CGH in Fresnel field, GS algorithm can be modified that replace the Fourier transform with the Fresnel transform[32]. In the book published recently, Tsang introduced methods of phase-only CGH for 3D object based on Fresnel transform.

1.3 Gerchberg-Saxton Algorithm

Gerchberg-Saxton algorithm(GSA) [20] is a phase retrieval algorithm which can be adopted in generating holograms of 2D images. This algorithm monotonically reduces the error of the amplitude of the reconstructed images each iteration [33], however, the efficiency reduces significantly with the further iteration.

The GSA can be modified into Fresnel field, which simply replace the Fourier transform with the Fresnel transform. Modified GS algorithm (MGSA) are designed for image compression and 3D CGH calculation.

1.4 Gradient Descent Algorithms

Gradient Descent algorithm, first invented by Cauchy in 1847, is a optimization iteration algorithm that reduce the loss function each iteration. Algorithms based on naive batch gradient descent are developeed recent years during the development of Deep Learning, which is called Gradient Descent Algorithms.

By calculating the gradient of the function and update the independent variable each iteration, the value of the function can be estimated to reduce mathematically. In the case of naive batch gradient descent algorithm, the effectiveness may reduce in some cases, algorithms like momentum, adagrad, RMSprop, adadelta, adam are developed to speed up the otimization.

Gradient Descent algorithms are widely used for optimizing. In the task of CGH, Gradient Descent Algorithms can also be adopted to generate the phase-only holograms or amplitude-only holograms, because the well defined and derivable loss function exists.

2 Gradient Descent Method Based Phase-only CGH for 2D Image Generation

2.1 Previous Research and Background

2.1.1 Gradient Descent method for phase-only holgrams

Gradient Descent method are not adopted for generating phase-only CGHs yet. However, the GS algorithm is equivalent as Gradient Descent method on consequent in math, which is proved by Fienup. Nonetheless, GS algorithm does not calculate the gradient of the error function. Thus, the GS algorithm is not a kind of Gradient Descent algorithm. Moreover, GS algorithm is equivalent as the Gradient Descent method which the error function is set as the mean square error of the amplitude of the regenerated image from the target image. However, the intensity of the light is equivalent as the square of the amplitude. Thus, the noise of the regenerated image is large in intensity.

2.1.2 Algorithms for Phase-only CGH generation

To generate the phase-only holograms of a target image, there are many other methods different from GS algorithm and GS based algorithms. Simulated annealing, time division method can also regenerate the image with a acceptable noise. Among the existing algorithms, GS algorithm produces the lowest error.

2.2 Gradient Descent Based CGH Algorithm

2.2.1 Gradient descent method for optimizing phase-only CGHs

The gradient descent algorithm is a first order iterative optimization algorithm which is committed to find a local minimum of a function. In order to find the local minimum, one takes steps toward the opposite direction of the gradient with a certain step length. Thus, there are two essential parts in the gradient descent method. The first part is the determination of the direction of the iteration, which is the opposite direction of the current gradient. The second part is the determination of the step length of the iteration. The formulated description of the gradient descent method is written by

$$\theta_{t+1} = \theta_t - \gamma_t \nabla F(\theta_t) \tag{1}$$

where t is the iteration number, γ_t is the step length coefficient of each iteration, and $\nabla F(\alpha_t)$ is the gradient of the function $F(\alpha)$.

This study considers the Fourier transform type phase-only CGHs, i.e., the Fourier transform of the phase distribution of the CGH provides the reconstructed image. The phase distribution of the CGH is denoted by θ_{pq}, where p and q represent the coordinates of the pixels on the hologram, and P and Q are the numbers of rows and columns of the hologram. The amplitude and phase distributions of the reconstructed image are denoted by a_{mn} and ϕ_{mn}, respectively, where m and n represent the coordinates of the pixels on the reconstructed image, and M and N are the numbers of rows and columns of the target image. The relationships between the phase-only CGH and the reconstructed image are given by:

$$a_{mn} e^{j\phi_{mn}} = \mathscr{F}\left\{e^{j\theta_{pq}}\right\} = \sum_{p}^{P}\sum_{q}^{Q} e^{j\theta_{pq}} e^{-j2\pi\left(\frac{mp}{P}+\frac{nq}{Q}\right)} \tag{2}$$

$$\mathscr{F}^{-1}\{a_{mn} e^{j\phi_{mn}}\} = \frac{1}{MN}\sum_{m}^{M}\sum_{n}^{N} a_{mn} e^{j\phi_{mn}} e^{j2\pi\left(\frac{mp}{M}+\frac{nq}{N}\right)} \tag{3}$$

The intensity distribution of the reconstructed image, denoted by I_{mn}, is given by:

$$I_{mn} = a_{mn}^2 \tag{4}$$

The gradient descent method calculates the gradient of the error of the reconstructed image. In this study, the MSE was adopted to evaluate the error of the reconstructed image. When the target image is denoted by $\hat{I}_{mn}$, the MSE is given by:

$$E = \frac{1}{MN}\sum_{m}^{M}\sum_{n}^{N}(\hat{I}_{mn} - I_{mn})^2 \tag{5}$$

The gradient of the MSE with respect to the phase distribution is calculated by the chain rule.

$$\frac{\partial E}{\partial \theta_{pq}} = \sum_{m}^{M}\sum_{n}^{N} \frac{\partial E}{\partial I_{mn}} \frac{\partial I_{mn}}{\partial \theta_{pq}} \tag{6}$$

$\frac{\partial E}{\partial I_{mn}}$ is calculated as follows:

$$\frac{\partial E}{\partial I_{mn}} = -\frac{2}{MN}(\hat{I}_{mn} - I_{mn}) \tag{7}$$

The following process shows the calculation of $\frac{\partial I_{mn}}{\partial \theta_{pq}}$:

$$I_{mn} = \left\{\sum_{p}^{P}\sum_{q}^{Q} \cos\left[\theta_{pq} - 2\pi\left(\frac{mp}{P} + \frac{nq}{Q}\right)\right]\right\}^2 + \left\{\sum_{p}^{P}\sum_{q}^{Q} \sin\left[\theta_{pq} - 2\pi\left(\frac{mp}{P} + \frac{nq}{Q}\right)\right]\right\}^2 \tag{8}$$

$$\begin{aligned}
\frac{\partial I_{mn}}{\partial \theta_{pq}} &= \frac{\partial\left\{\sum_{p}^{P}\sum_{q}^{Q} \cos\left[\theta_{pq} - 2\pi\left(\frac{mp}{P} + \frac{nq}{Q}\right)\right]\right\}^2}{\partial \theta_{pq}} + \frac{\partial\left\{\sum_{p}^{P}\sum_{q}^{Q} \sin\left[\theta_{pq} - 2\pi\left(\frac{mp}{P} + \frac{nq}{Q}\right)\right]\right\}^2}{\partial \theta_{pq}} \\
&= -2\left\{\sum_{p}^{P}\sum_{q}^{Q} \cos\left[\theta_{pq} - 2\pi\left(\frac{mp}{P} + \frac{nq}{Q}\right)\right]\right\} \sin\left[\theta_{pq} - 2\pi\left(\frac{mp}{P} + \frac{nq}{Q}\right)\right] \\
&\quad + 2\left\{\sum_{p}^{P}\sum_{q}^{Q} \sin\left[\theta_{pq} - 2\pi\left(\frac{mp}{P} + \frac{nq}{Q}\right)\right]\right\} \cos\left[\theta_{pq} - 2\pi\left(\frac{mp}{P} + \frac{nq}{Q}\right)\right] \\
&= -2\mathrm{Re}\left\{a_{mn} e^{j\phi_{mn}}\right\} \sin\left[\theta_{pq} - 2\pi\left(\frac{mp}{P} + \frac{nq}{Q}\right)\right] \\
&\quad + 2\mathrm{Im}\left\{a_{mn} e^{j\phi_{mn}}\right\} \cos\left[\theta_{pq} - 2\pi\left(\frac{mp}{P} + \frac{nq}{Q}\right)\right] \\
&= -2a_{mn}\cos\phi_{mn} \sin\left[\theta_{pq} - 2\pi\left(\frac{mp}{P} + \frac{nq}{Q}\right)\right] + 2a_{mn}\sin\phi_{mn} \cos\left[\theta_{pq} - 2\pi\left(\frac{mp}{P} + \frac{nq}{Q}\right)\right] \\
&= 2a_{mn}\sin\left[\phi_{mn} - \theta_{pq} + 2\pi\left(\frac{mp}{P} + \frac{nq}{Q}\right)\right]
\end{aligned} \tag{9}$$

Then, the gradient of the MSE is given as follows:

$$\frac{\partial E}{\partial \theta_{pq}} = \frac{4}{MN}\sum_{m}^{M}\sum_{n}^{N}\left(\hat{I}_{mn} - a_{mn}^2\right) a_{mn} \sin\left[\phi_{mn} - \theta_{pq} + 2\pi\left(\frac{mp}{P} + \frac{nq}{Q}\right)\right] \tag{10}$$

The above calculation can be described using the Fourier transform.

$$\begin{aligned}\frac{\partial E}{\partial \theta_{pq}} &= \frac{4}{MN}\mathrm{Im}\left\{\sum_{m}^{M}\sum_{n}^{N}\left(\hat{I}_{mn}-a_{mn}^{2}\right)a_{mn}e^{j\left[\phi_{mn}-\theta_{pq}+2\pi\left(\frac{mp}{P}+\frac{nq}{Q}\right)\right]}\right\} \\ &= \frac{4}{MN}\mathrm{Im}\left\{e^{-j\theta_{pq}}\sum_{m}^{M}\sum_{n}^{N}\left(\hat{I}_{mn}-a_{mn}^{2}\right)a_{mn}e^{j\left[\phi_{mn}+2\pi\left(\frac{mp}{P}+\frac{nq}{Q}\right)\right]}\right\}\end{aligned} \tag{11}$$

Substitute the Fourier Transform (3) into (11).

$$\frac{\partial E}{\partial \theta_{pq}} = -4\mathrm{Im}\left\{e^{-j\theta_{pq}}\mathscr{F}^{-1}\left[\left(\hat{I}_{mn}-a_{mn}^{2}\right)a_{mn}e^{j\phi_{mn}}\right]\right\} \tag{12}$$

where $\mathscr{F}^{-1}$ represents the Fourier transform. When the fast Fourier transform algorithm is used, the calculation time can be reduced.

According to the gradient descent method, the phase distribution is updated each iteration as follows:

$$\theta_{pq}^{'} = \theta_{pq} + \Delta\theta_{pq} = \theta_{pq} - \gamma\frac{\partial E}{\partial \theta_{pq}} \tag{13}$$

2.2.2 Determination of step length coefficient

Next, the determination of the step length coefficient is explained. In this study, the coefficient is determined using the estimated MSE of the next iteration.

The MSE of the next iteration is estimated as below.

$$E^{'} = \sum_{m}^{M}\sum_{n}^{N}\frac{\left[\hat{I}_{mn}-\left(I_{mn}+\Delta I_{mn}\right)\right]^{2}}{MN} \tag{14}$$

where ΔI_{mn} is the estimated direction for the phase change $\Delta\theta_{pq}$. The step length coefficient γ is determined so that $E^{'}$ becomes minimum, i.e., $\frac{dE^{'}}{d\gamma}=0$

$$E^{'} = \frac{1}{MN}\sum_{m}^{M}\sum_{n}^{N}\left[\left(\hat{I}_{mn}-a_{mn}^{2}\right)-\Delta I_{mn}\right]^{2} \tag{15}$$

$$\frac{\partial E^{'}}{\partial \gamma} = \frac{2}{MN}\sum_{m}^{M}\sum_{n}^{N}\left[\left(\hat{I}_{mn}-a_{mn}^{2}\right)-\Delta I_{mn}\right]\left(-\frac{\partial \Delta I_{mn}}{\partial \gamma}\right)=0 \tag{16}$$

We can adopt the first order approximation to calculate ΔI_{mn}

$$\Delta I_{mn} \approx \sum_{p}^{P}\sum_{q}^{Q}\frac{\partial I_{mn}}{\partial \theta_{pq}}\Delta\theta_{pq} \tag{17}$$

Substrate (9) into (17)

$$\begin{aligned}\Delta I_{mn} &\approx \sum_{p}^{P}\sum_{q}^{Q} 2a_{mn}\Delta\theta_{pq}\sin\left[\phi_{mn}-\theta_{pq}+2\pi\left(\frac{mp}{P}+\frac{nq}{Q}\right)\right] \\ &\approx 2\mathrm{Im}\left\{a_{mn}e^{j\phi_{mn}}\sum_{p}^{P}\sum_{q}^{Q}\Delta\theta_{pq}e^{-j\left[\theta_{pq}-2\pi\left(\frac{mp}{P}+\frac{nq}{Q}\right)\right]}\right\}\end{aligned} \tag{18}$$

Substrate (2) into (18)

$$\Delta I_{mn} \approx 2\mathrm{Im}\left\{a_{mn}e^{j\phi_{mn}}\left[\mathscr{F}\left(\Delta\theta_{pq}e^{j\theta_{pq}}\right)\right]^{*}\right\} = 2\gamma\mathrm{Im}\left\{a_{mn}e^{j\phi_{mn}}\left[\mathscr{F}\left(-\frac{\partial E}{\partial\theta_{pq}}e^{j\theta_{pq}}\right)\right]^{*}\right\} \tag{19}$$

Substrate (19) into (16).

$$\frac{2}{MN}\sum_{m}^{M}\sum_{n}^{N}\left[\left(\hat{I}_{mn}-a_{mn}^{2}\right)-2\gamma\mathrm{Im}\left\{a_{mn}e^{j\phi_{mn}}\left[\mathscr{F}\left(-\frac{\partial E}{\partial\theta_{pq}}e^{j\theta_{pq}}\right)\right]^{*}\right\}\right]\left[-2\mathrm{Im}\left\{a_{mn}e^{j\phi_{mn}}\left[\mathscr{F}\left(-\frac{\partial E}{\partial\theta_{pq}}e^{j\theta_{pq}}\right)\right]^{*}\right\}\right] = 0 \tag{20}$$

Finally, γ is determined as follows:

$$\gamma = \frac{\sum_{m}^{M}\sum_{n}^{N}(\hat{I}_{mn}-a_{mn}^{2})\mathrm{Im}\left\{a_{mn}e^{j\phi_{mn}}\left[\mathscr{F}\left(-\frac{\partial E}{\partial\theta_{pq}}e^{j\theta_{pq}}\right)\right]^{*}\right\}}{2\sum_{m}^{M}\sum_{n}^{N}\left[\mathrm{Im}\left\{a_{mn}e^{j\phi_{mn}}\left[\mathscr{F}\left(-\frac{\partial E}{\partial\theta_{pq}}e^{j\theta_{pq}}\right)\right]^{*}\right\}\right]^{2}} \tag{21}$$

By determining the step length in each iteration, we can obtain a nearly optimal step length coefficient which makes the MSE reduce rapidly.

Figure 1 shows the phase-only CGH calculation process based on the theory described above. A random phase distribution is used as an initial phase distribution of the CGH. The phase-only CGH is Fourier transformed to obtain the reconstruct the image, which is multiplied by the difference of the intensity distributions of the reconstructed image and the target image. Next, the inverse Fourier transform is performed and the phase distribution of the CGH of the previous iteration is multiplied. Then, the imaginary part is extracted and –4 is multiplied to obtain the gradient. The step length coefficient is calculated to calculate the increment of the phase distribution. Finally, the phase distribution of the CGH is updated. This process is performed interactively.

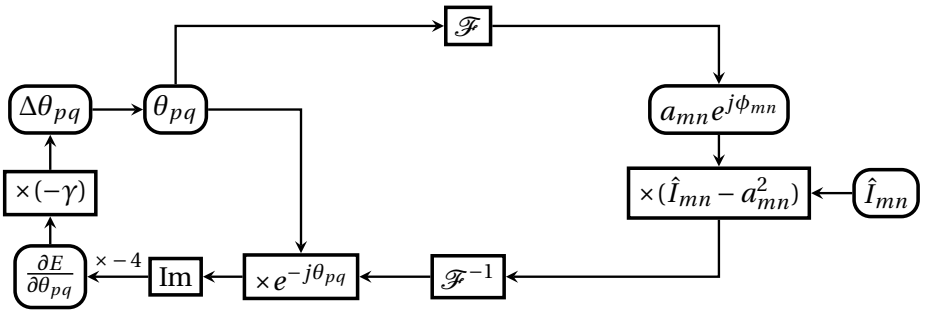

Figure 1: Calculation process of the proposed technique.

2.3 Simulation

The effectiveness of the proposed algorithm was verified. Figure 2 shows three target images including one grayscale image ("mandrill") and two binary images ("hikari" and "circle").

(a) Mandrill (b) Hikari (c) Circle

Figure 2: Target images

The reconstructed images obtained by the proposed technique for "hikari" after 1, 2, 5, 10, 50, and 100 iterations are shown in Figure 3. For comparisons, the reconstructed images obtained by the GS algorithm are shown in Figure 4. From these results, the proposed technique required fewer iterations for the phase optimization.

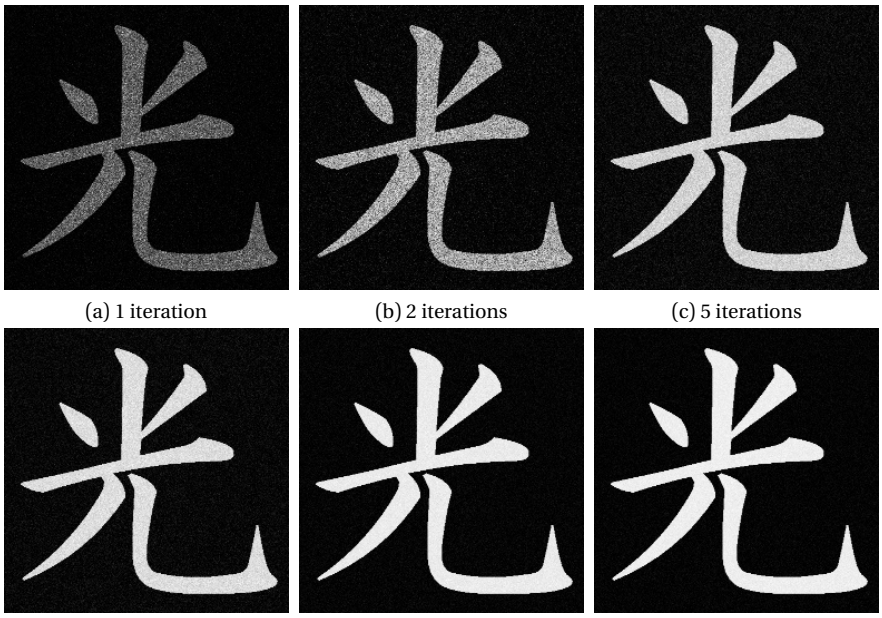

(a) 1 iteration (b) 2 iterations (c) 5 iterations

(d) 10 iterations (e) 50 iterations (f) 100 iterations

Figure 3: Images(hikari) reconstructed by proposed algorithm

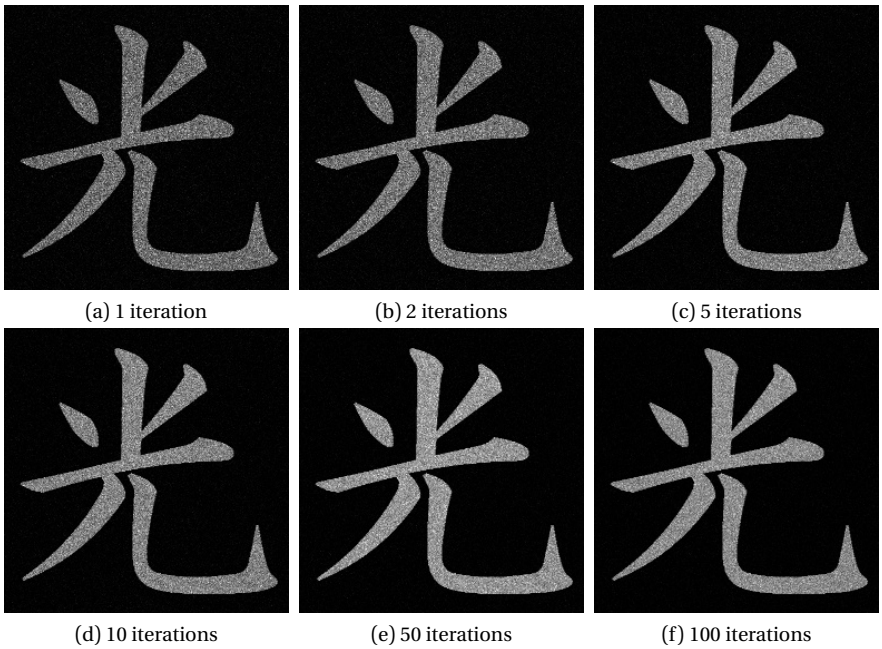

(a) 1 iteration (b) 2 iterations (c) 5 iterations

(d) 10 iterations (e) 50 iterations (f) 100 iterations

Figure 4: Images(hikari) reconstructed by GS algorithm

Figure 5 shows the reconstructed images and the phase-only CGHs for the three target images after 100 iterations obtained for the proposed technique and the GS

technique. The changes of the MSE during the optimization process are shown in Figure 6. From these results, the lower MSE values were obtained with the proposed algorithm than the conventional GS algorithm.

(a) Mandrill by proposed algorithm (b) Hikari by proposed algorithm (c) Circle by proposed algorithm

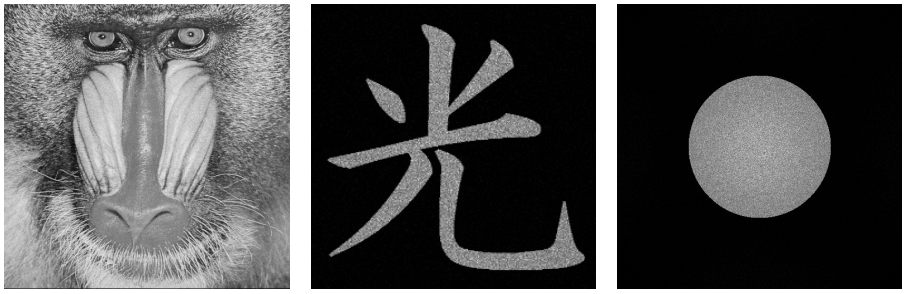

(d) Mandrill by GS algorithm (e) Hikari by GS algorithm (f) Circle by GS algorithm

Figure 5: Comparison of proposed technique and GS technique

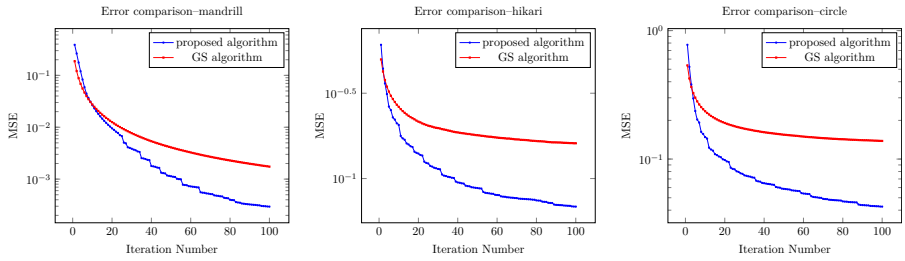

(a) Mandrill (b) Hikari (c) Circle

Figure 6: Comparison of MSE of 3 target images

The surface images of the reconstructed images for “circle” after 100 iterations obtained by the proposed algorithm and the GS algorithm are shown in Figure 7, respectively. From these results, the proposed algorithm controlled the intensity distribution of the reconstructed image than the GS algorithm.

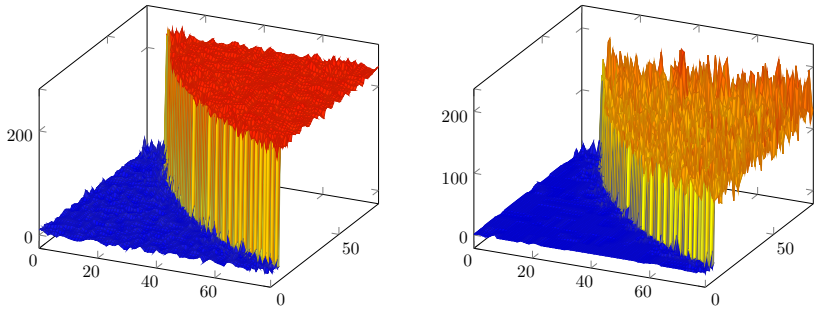

(a) Reconstructed by proposed algorithm (b) Reconstructed by GS algorithm

Figure 7: Surface image of a part of "circle"

Finally, the effectiveness of the step length optimization algorithm was verified. Constant step length coefficients were used for the proposed algorithm. Figure 8 shows the comparison of the algorithm using constant step length coefficient and the algorithm using the optimized step length coefficient. As the result of different target image, a best step length constant does not exist. The optimized step length algorithm can do well in different target images.

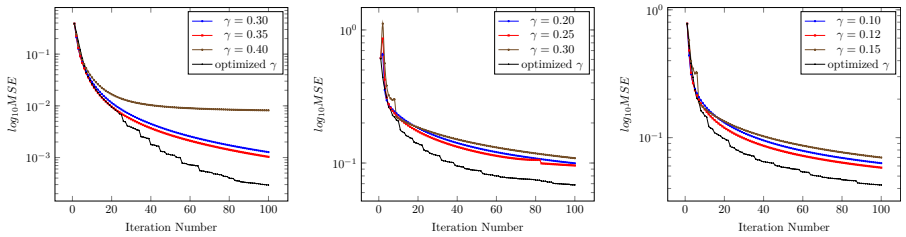

(a) Mandrill (b) Hikari (c) Circle

Figure 8: The comparison of the constant and the optimized step length coefficient

2.4 Experimental Results

The proposed technique was experimentally verified utilizing the experimental system shown in Figure 9. A PLUTO-2 phase-only SLM (HOLOEYE Photonics AG) was utilized, and a He-Ne laser with a wavelength of 633 nm was used as the light source. The focal length of the Fourier transform lens was 450 mm.

Figures 10a – 10c show the phase distributions used for the experiments, which correspond to the reconstructed images shown in Figures 5. The experimentally obtained reconstructed images are shown in Figures 11a – 11c.

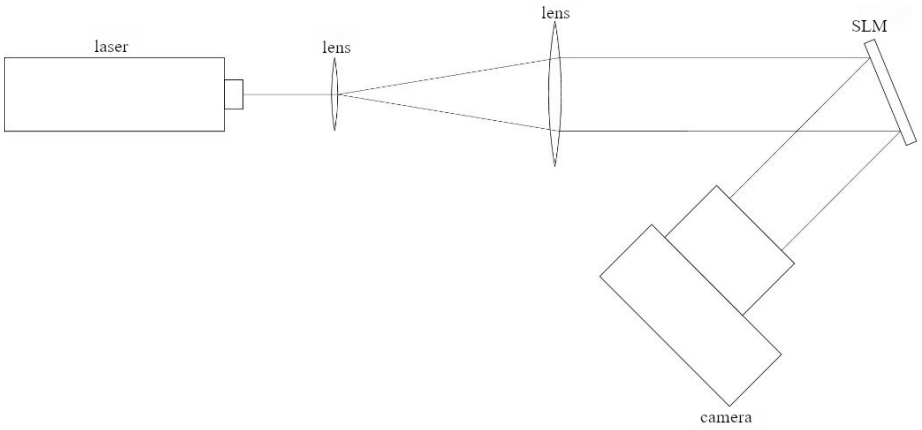

Figure 9: Experimental system

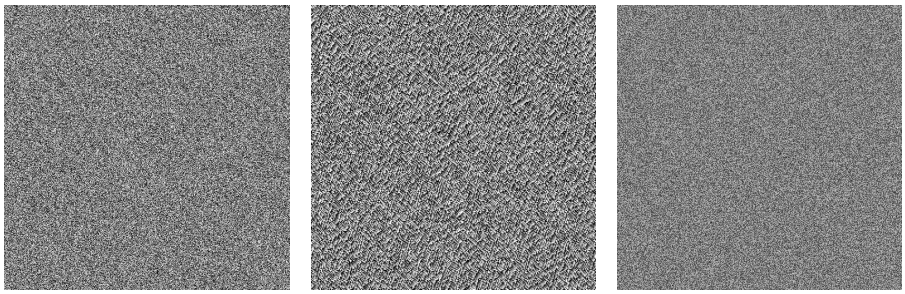

(a) Mandrill (b) Hikari (c) Circle

Figure 10: Optimized phase distributions used for the experiments for the different target images: (a) mandrill, (b) hikari, and (c) circle

(a) Mandrill (b) Hikari (c) Circle

Figure 11: Experimentally obtained reconstructed images for the different target images: (a) mandrill, (b) hikari, and (c) circle

From Figure 11, the test images were reconstructed. However, the reconstructed images contained speckles because the phase distributions of the reconstructed

images were not controlled. Although the images “hikari” and “circle” were reconstructed clearly, the image “mandrill” was not as clear as them. Because the “hikari” and “circle” were binary images, the image contrast was not affected so much by the speckles. On the contrary, because the “mandrill” was a gray-scale image, the image contrast was heavily affected.

2.5 Discussion

A new technique was proposed for calculating phase-only CGHs using the gradient descent method, which minimizes the MSE defined for the intensity distributions of reconstructed images. We confirmed that the proposed technique optimizes the CGH phase distribution more rapidly than the GS algorithm and provides higher-precision reconstructed images. The proposed technique was also experimentally verified.

3 Gradient Descent Method Based Phase-only CGH of 3D Image

3.1 Previous Research and Background

There are two main approximation methods in physics for diffraction. Fraunhofer diffraction, also known as far field diffraction, which reconstruct the image on the observation plane far enough from the hologram. With the utilization of a Fourier transform lens, the reconstructed image is located at the Fourier plane (focal plane). This enables the objective plane to locate at a near position from the hologram. Many algorithms produce the holograms in Fourier field, such as simulated annealing, genetic algorithms, machine learning algorithms, Gerchberg-Saxton (GS) algorithm, gradient descent algorithm, etc. However, Fourier transform based CGH produces only the hologram of 2D image.

Fresnel diffraction, known as near field diffraction, which reconstructs the image on the observation plane directly. CGHs of Fresnel field are able to produce holograms that can reconstruct 3D images. Various researches focus on developing phase only CGH algorithms in Fresnel field. However, due to the pixel pitch of the SLMs at present are too big comparing with the wavelength of the lasers, the near field of Fresnel transform is still too long in practice. Thus, a new transform is desired for CGHs for regenerating 3D images with the utilization of the Fourier transform lens for a nearer imaging position and a larger field of view. Such transform would realize portable designs of 3D display systems.

Gradient Descent is an optimization method that reduces the error by changing the variant opposite the gradient each iteration. Gradient Descent algorithms are widely used in deep learning in recent years. Gradient Descent based algorithm for phase only CGH was proposed in previous research, which showed a higher efficiency and precision. In this research, we propose a Gradient Descent based algorithm for phase only CGH of 3D images with the utilization of a Fresnel transform lens.

3.2 Design of Fresnel Transform with the Utilization of Fourier Lens

3.2.1 Diffraction based on the Fourier transform

In the field of Fraunhofer diffraction, also known as far field diffraction, the image reconstructed in the screen in far field. The reconstructed image is the Fourier transform of the holograph. We can also adopt an Fourier transfrom lens to reconstructed image on the Fourier plane[34]. The light diffraction is given by the Fourier transform as below:

$$E'(x',y') = \frac{e^{i\frac{2\pi f}{\lambda}}}{i\lambda f}\iint_{-\infty}^{+\infty} E(x,y)e^{-i\frac{2\pi}{\lambda f}(x'x+y'y)}dxdy \tag{22}$$

where λ is the wavelength of light, the object plane is denoted by (x,y), and the diffraction plane is denoted by $(x\square, y\square)$. The distribution of a 2D object located on the object plane is denoted by $E(x,y)$, and the distribution on the diffraction plane is denoted by $E\square(x\square, y\square)$. A point at (x,y) on the object plane generates a plane wave $e^{-i\frac{2\pi}{\lambda f}(xx'+yy')}$on the diffraction plane. The inclination of the plane wave depends on the position of the point (x,y) on the object plane and is given by $(\frac{2\pi x}{\lambda f}, \frac{2\pi y}{\lambda f})$.

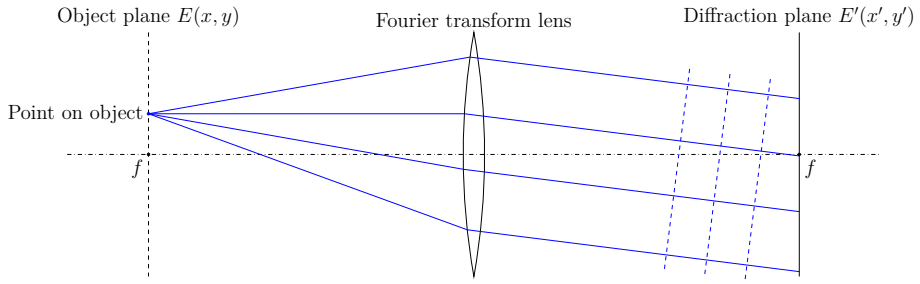

Figure 12: Hologram Generation by Fourier transform

3.2.2 Diffraction based on the Fresnel transform

In the field of Fresnel diffraction, also known as near field diffraction, the image reconstructed in the near field without a utilization of Fourer transform lens. The optical system of the diffraction is whown as Figure 13. The function of Fresnel transform is shown as below:

$$E'(x',y') = \iint_{-\infty}^{+\infty} E(x,y,0)\frac{e^{i\frac{2\pi z}{\lambda}}}{i\lambda z} e^{i\frac{\pi}{\lambda z}\left[(x'-x)^2+(y'-y)^2\right]} \tag{23}$$

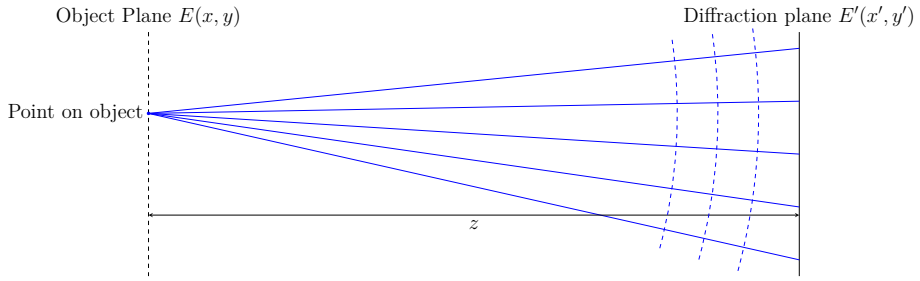

Figure 13: Hologram Generation by Fresnel transform

3.2.3 Diffraction based on the Fresnel transform with the utilization of Fourier lens

Both holograms based on Fourier and Fresnel transforms have disadvantages. Holograms based on Fourier transform does not have the capability of regenerating 3D images. Holgrams based on Fresnel transforms can regenerate the 3D images, but the "near field" in practice is too far. Moreover, the precision of SLM at present does not support a high resolution with the Fresnel transform. Thus, a new transform is desired to reconstruct 3D images with the optical system of Fourier transform.

A Fresnel transform with the utilization of Fourier lens is proposed for 3D holograms. The optical system is shown as Figure 14

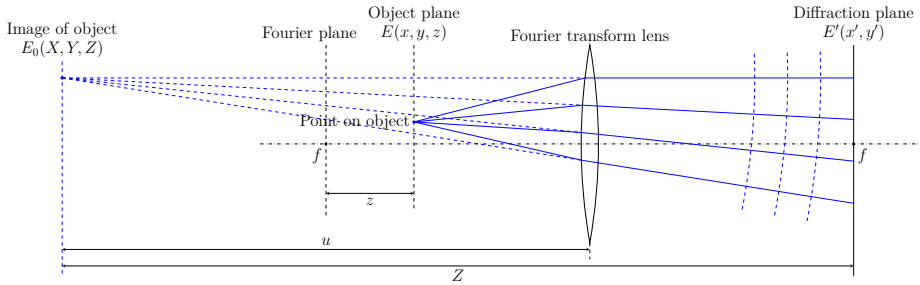

Figure 14: Optical system of the proposed transform

Where u is the image distance and Z is the distance of the image from the diffraction plane. X, Y, Z is the coordinates of the image of the object.

The Fourier transform lens produces the virtual image of the 3D object far from

the Fourier transform lens. Considering the Fresnel transform represented by Eq. (23), the electric field of each point on the virtual image is $E_0(X,Y,Z)$. The convert of the electric field of the object and the virtual image is explained as following.

The image distance u can be calculated through the convex lens imaging formula.

$$u = \frac{f}{z}(f-z) \tag{24}$$

The convert relation of the coordinate X,Y and x,y is shown as below:

$$\begin{aligned} \frac{X}{u} &= \frac{x}{f-z}, \quad & \frac{Y}{u} &= \frac{y}{f-z}. \\ X &= \frac{f}{z}x, & Y &= \frac{f}{z}. \end{aligned} \tag{25}$$

The convert relation of the depth distance Z and z is shown as below:

$$Z = u + f = \frac{f^2}{z} \tag{26}$$

The convert relation of the electric field of the object $E(x,y,z)$ and virtual image $E_0(X,Y,Z)$ is divided by amplitude convert and phase convert. The electric field can be expressed as:

$$\begin{aligned} E(x,y,z) &= A(x,y,z)e^{i\theta(x,y,z)} \\ E_0(X,Y,Z) &= A_0(X,Y,Z)e^{i\theta_0(X,Y,Z)} \end{aligned} \tag{27}$$

where $A(x,y,z)$ and $A_0(X,Y,Z)$ are the amplitude of the object and the virtual image. $\theta(x,y,z)$ and $\theta_0(X,Y,Z)$ are the phase of the object and the virtual image.

We first consider the amplitude relation of the object and the virtual image. The virtual image and the object show a same light intensity on the center of the Fourier transform lens.

$$\frac{A(x,y,z)\,dx\,dy}{f-z} = \frac{A_0(X,Y,Z)\,dX\,dY}{u} \tag{28}$$

The differential relation can be inferred from Eq. (25)

$$dX = \frac{f}{z}dx, dY = \frac{f}{z}dy \tag{29}$$

Substrate the Eqs. (24) and (29) into Eq. (28), the amplitude convert can be expressed as following:

$$A_0(X,Y,Z)\,dX\,dY = \frac{f}{z}A(x,y,z)\,dx\,dy \tag{30}$$

The phase convert can be calculated by the distance of the object and the virtual image.

$$\theta(x,y,z) - \theta_0(X,Y,Z) = \frac{2\pi}{\lambda}\sqrt{[u-(f-z)]^2 + (X-x)^2 + (Y-y)^2} \tag{31}$$

Substrate the Eqs. (24) and (25) into Eq. (31), the first-order approximation is

$$\theta(x,y,z) - \theta_0(X,Y,Z) = \frac{2\pi}{\lambda z}(f-z)^2 + \frac{\lambda}{\pi z}(x^2+y^2) \tag{32}$$

The Fresnel diffraction of the virtual image can be expressed as below

$$E'(x',y') = \iint_{-\infty}^{+\infty} E_0(X,Y,Z)\frac{e^{i\frac{2\pi}{\lambda}Z}}{i\lambda Z}e^{i\frac{\pi}{\lambda Z}\left[(X-x')^2+(Y-y')^2\right]}dX\,dY \tag{33}$$

Change the expression of the Eq. (33) into amplitude and phase:

$$E'(x',y') = \iint_{-\infty}^{+\infty} A_0(X,Y,Z)e^{i\theta_0(X,Y,Z)}\frac{e^{i\frac{2\pi}{\lambda}Z}}{i\lambda Z}e^{i\frac{\pi}{\lambda Z}\left[(X-x')^2+(Y-y')^2\right]}dX\,dY \tag{34}$$

Substrate $X,Y,Z,A_0(X,Y,Z)\,dX\,dY,\theta_0(X,Y,Z)$ into function Eq. (34)

$$E'(x',y') = \iint_{-\infty}^{+\infty} A(x,y,z)e^{i\theta(x,y,z)}\frac{e^{i\frac{2\pi}{\lambda}(2f-z)}}{i\lambda f}e^{-i\frac{2\pi}{\lambda f}(xx'+yy')}e^{i\frac{\pi z}{\lambda f^2}(x'^2+y'^2)}dx\,dy \tag{35}$$

Thus, the Fresnel transform with the utilization of Fourier lens can be expressed as below:

$$E'(x',y') = \iint_{-\infty}^{+\infty} E(x,y,z)\frac{e^{i\frac{2\pi}{\lambda}(2f-z)}}{i\lambda f}e^{-i\frac{2\pi}{\lambda f}(xx'+yy')}e^{i\frac{\pi z}{\lambda f^2}(x'^2+y'^2)}dx\,dy \tag{36}$$

The transform above possesses a counter part of the Fourier transform, $e^{-i\frac{2\pi}{\lambda f}(xx\prime+yy\prime)}$, which is phase distribution of a plane wave. The main difference of the transform above and the Fourier transform is $e^{i\frac{\pi z}{\lambda f^2}\left(x'^2+y'^2\right)}$, which is a phase distribution of a

centralized spherical wave. When the object point is nearer to the lens, the depth coordinate $z(x,y)$ is positive, where the spherical wave is divergence (Fig. 15). When the object point is farther to the lens, the depth coordinate $z(x,y)$ become negative, the phase diffraction of the spherical wave is converging (Fig. 16).

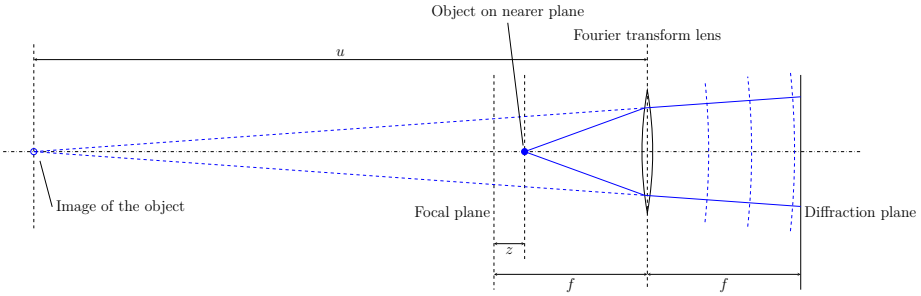

Figure 15: Object on nearer plane

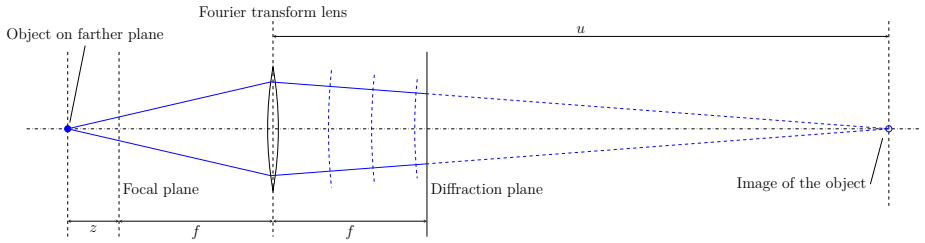

Figure 16: Object on farther plane

Similar to the inverse Fresnel transform, the inverse transform of the transform above is expressed as below:

$$E(x,y,z) = \frac{1}{2\pi}\iint_{-\infty}^{+\infty} E'(x',y')i\lambda f e^{-i\frac{2\pi}{\lambda}(2f-z)} e^{i\frac{2\pi}{\lambda f}(xx'+yy')} e^{-i\frac{\pi z}{\lambda f^2}(x'^2+y'^2)} dx'dy' \quad (37)$$

3.2.4 Computer simulations of proposed transform

The computer simulations were performed to verify the inversibility of the proposed transforms and the accuracy of the diffraction calculation.

The discrete form of the proposed transform and inverse transform can be proposed through a convert relation. The SLM is located at the diffraction plane. Thus, the coordinates of the diffraction side can be expressed as:

$$
\begin{aligned}
x' &= p_0 p \left(-\frac{P}{2} \le p \le \frac{P}{2} - 1 \right) \\
y' &= p_0 q \left(-\frac{Q}{2} \le p \le \frac{Q}{2} - 1 \right)
\end{aligned}
\tag{38}
$$

where p and q are the row and column coordinates of the SLM, and P and Q are the numbers of rows and columns, and p_0 is the pixel pitch of the SLM.

Consider the object side, the size of the object was limited in the effective range. The effective row and column ranges are determined by the pixel pitch.

$$
l_0 = \frac{f\lambda}{p_0} \tag{39}
$$

where l_0 is the effective row and column length of the object.

We set the same row, column, and depth ranges. Thus, the convert relation of the object coordinate is:

$$
\begin{aligned}
x &= l_0 \frac{m}{M} = \frac{f\lambda}{p_0}\frac{m}{M} \quad \left(-\frac{M}{2} \le m \le \frac{M}{2} - 1 \right) \\
y &= l_0 \frac{n}{N} = \frac{f\lambda}{p_0}\frac{n}{N} \quad \left(-\frac{N}{2} \le n \le \frac{N}{2} - 1 \right) \\
z &= \frac{l_0}{2} z_{mn} = \frac{f\lambda}{2p_0} z_{mn} \quad (-1 \le z_{mn} \le 1)
\end{aligned}
\tag{40}
$$

where m and n are row and column coordinates of the object, and M and N are the numbers of the rows and columns, and z_{mn} is the relative depth position of the object.

Substrate the coordinates into the proposed transform. The discrete form of the proposed transform can be expressed as below.

$$
A'_{pq} e^{i\theta'_{pq}} = \sum_{m=-\frac{M}{2}}^{\frac{M}{2}-1} \sum_{n=-\frac{N}{2}}^{\frac{N}{2}-1} A_{mn} e^{i\theta_{mn}} e^{i\frac{2\pi}{\lambda}\left(2f - \frac{f\lambda}{2p_0} z_{mn}\right)} e^{-i2\pi\left(\frac{mp}{M} + \frac{nq}{N}\right)} e^{i\frac{\pi p_0}{2f} z_{mn}(p^2+q^2)} \tag{41}
$$

Similar to the inverse Fresnel transform, the inverse transform is shown as below:

$$A_{mn}e^{i\theta_{mn}} = \frac{1}{PQ}\sum_{p=-\frac{P}{2}}^{\frac{P}{2}-1}\sum_{q=-\frac{Q}{2}}^{\frac{Q}{2}-1} A'_{pq}e^{i\theta'_{pq}}e^{-i\frac{2\pi}{\lambda}\left(2f-\frac{f\lambda}{2p_0}z_{mn}\right)}e^{i2\pi\left(\frac{mp}{M}+\frac{nq}{N}\right)}e^{-i\frac{\pi p_0}{2f}z_{mn}(p^2+q^2)} \tag{42}$$

Eq. (42) can also be expressed as:

$$A_{mn}e^{i\theta_{mn}}e^{i\frac{2\pi}{\lambda}\left(2f-\frac{f\lambda}{2p_0}z_{mn}\right)} = \frac{1}{PQ}\sum_{p=-\frac{P}{2}}^{\frac{P}{2}-1}\sum_{q=-\frac{Q}{2}}^{\frac{Q}{2}-1} A'_{pq}e^{i\theta'_{pq}}e^{i2\pi\left(\frac{mp}{M}+\frac{nq}{N}\right)}e^{-i\frac{\pi p_0}{2f}z_{mn}(p^2+q^2)} \tag{43}$$

There is a common item in Eqs. (41) and (43), $e^{i\theta_{mn}}e^{i\frac{2\pi}{\lambda}\left(2f-\frac{f\lambda}{2p_0}z_{mn}\right)}$, which is the phase of the object and a phase compensation determined by the depth coordination. We can substitute this item with $e^{i\varphi_{mn}}$:

$$\begin{aligned}\varphi_{mn} &= \theta_{mn} + \frac{2\pi}{\lambda}\left(2f - \frac{f\lambda}{2p_0}z_{mn}\right)\\ e^{i\varphi_{mn}} &= e^{i\theta_{mn}+\frac{2\pi}{\lambda}\left(2f-\frac{f\lambda}{2p_0}z_{mn}\right)}\end{aligned} \tag{44}$$

The discrete transform and inverse transform can be thus expressed as following:

$$A'_{pq}e^{i\theta'_{pq}} = \mathcal{T}(A_{mn}e^{i\theta mn}, z_{mn}) = \sum_{m=-\frac{M}{2}}^{\frac{M}{2}-1}\sum_{n=-\frac{N}{2}}^{\frac{N}{2}-1} A_{mn}e^{i\varphi_{mn}}e^{-i2\pi\left(\frac{mp}{M}+\frac{nq}{N}\right)}e^{i\frac{\pi p_0}{2f}z_{mn}(p^2+q^2)} \tag{45}$$

$$A_{mn}e^{i\varphi_{mn}} = \mathcal{T}^{-1}(A'_{pq}e^{i\theta'_{pq}}, z_{mn}) = \frac{1}{PQ}\sum_{p=-\frac{P}{2}}^{\frac{P}{2}-1}\sum_{q=-\frac{Q}{2}}^{\frac{Q}{2}-1} A'_{pq}e^{i\theta'_{pq}}e^{i2\pi\left(\frac{mp}{M}+\frac{nq}{N}\right)}e^{-i\frac{\pi p_0}{2f}z_{mn}(p^2+q^2)} \tag{46}$$

The proposed transform and inverse transform cannot be applied as fast Fourier transform (FFT) because the proposed transform is equivalent as Fresnel transform for 3D object, which cannot be applied the fast transform.

The conventional algorithms based on Fourier or Fresnel transforms are point-based methods that each point stand for a pixel. However, most of the phase only CGHs are based on Fourier or Fresnel transforms. The main advantage over the

layered Fourier transform is the optimization algorithm. The layered Fourier transform based phase only CGH algorithm so far does not able to optimize the whole image on different layers simultaneously, optimization of a certain layer may bring extra error to other layers. Thus, more layers bring bigger error. The proposed transform in this paper enables the optimization algorithm optimizes the image on a certain 3D surface, this enables the advantage over the layered Fourier transform that image parts on all the layers could be optimized simultaneously.

The adopted SLM in experiments is PLUTO-2.1 LCOS Spatial Light Modulator Phase Only (Reflective) (HOLOEYE Photonics AG). The pixel pitch is 8 μm. The resolution is 1,080 × 1,920. The focal distance of the Fourier transform lens is 150 mm. The adopted laser is a He-Ne laser with the wavelength of 632.8nm.

We did the simulation to test the proposed transform. We adopted two images with different depth option (Figs. 17 and 18), which the resolution was 300×300. In the "$\mathscr{LR}$" image (Fig. 17), the letter "$\mathscr{L}$" is located on the preset minimum range to the Fourier transform lens; the letter "$\mathscr{R}$" is in the preset maximum range to the Fourier transform lens. In the "grid" image (Fig. 18), the depth option is an inclined screen.

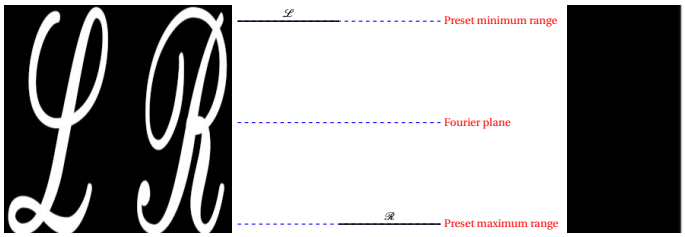

Figure 17: "$\mathscr{LR}$" image, depth option and image of depth option

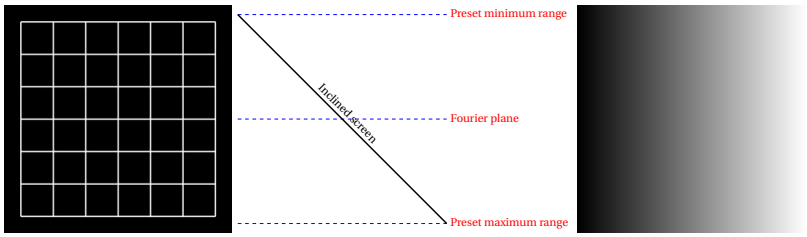

Figure 18: "grid" image, depth option and image of depth option

To test the validity of the proposed algorithm, such simulation was executed that do the inverse transform of the transform of the image. The desired result is

that the inverse transform reconstructs the target image on the depth position from the transform of the target image and all the pixels are focused. Figure 8 shows the transform of the "$\mathscr{LR}$" image with a random phase which the resolution was changed to 1,920×1,080 to fit the SLM adopted in the experiment. Fig. 20 shows the reconstructed image by making the inverse transform of the Fig. 19. Fig. 21 shows the transform of the "grid" image with a random phase, and Fig. 22 shows the reconstructed image.

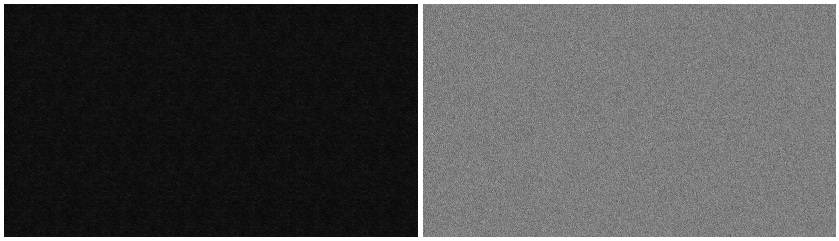

Figure 19: Transform of the "$\mathscr{LR}$" image. Left: Intensity; Right: phase (1920×1080)

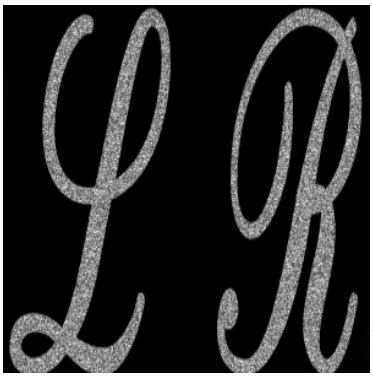

Figure 20: Reconstructed "$\mathscr{LR}$" image (300×300)

Figure 21: Transform of the "grid" image. Left: Intensity; Right: phase (1920×1080)

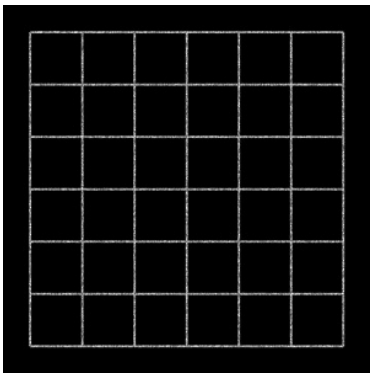

Figure 22: Reconstructed “grid” image (300×300)

The validity of the porposed transform is confirmed through the computer simulations. The image reconstructed correctly after the proposed transform and then inverse transform. The transform cosumes about 70 seconds each time.

3.3 Gradient-Descent Method Based 3D Phase-Only CGH Algorithm

I tried to construct gradient-descent based method as the section 2 did. If we simply replace the Fourier transform with the proposed transform, the theoretical validity cannot be confirmed and the error cannot be estimated. The mathematical verification of the gradient-descent based 3D phase-only CGH algorithm is shown as below.

To calculate the hologram of a 3D image, the method of gradient descent can be utilized. Similar to the former research, there are two essential elements in gradient descent method, which are error estimation function and the gradient of the error and the retrieval variant.

In this research, we set the error estimation function as the Mean Square Error of the intensity of the regenerated image and the target image. The retrieval variant is the phase distribution of the hologram.

The gradient of the error and the retrieval variant can be calculated through chain rule 47.

$$\frac{\partial E}{\partial \theta'_{pq}} = \sum_{m=-\frac{M}{2}}^{\frac{M}{2}-1} \sum_{n=-\frac{N}{2}}^{\frac{N}{2}-1} \frac{\partial E}{\partial I_{mn}} \frac{\partial I_{mn}}{\partial \theta'_{pq}} \tag{47}$$

where θ'_{pq} is the phase of the pixel p and q on the hologram.

The equation 47 can be calculated separately.

calculation of $\frac{\partial E}{\partial I_{mn}}$:

$$\frac{\partial E}{\partial I_{mn}} = \frac{2}{\bar{I}MN}\left(\frac{I_{mn}}{\bar{I}} - \frac{I_{0-mn}}{\bar{I}_0}\right) \tag{48}$$

calculation of $\frac{\partial I_{mn}}{\partial \theta'_{pq}}$:

The intensity of the regenerated image can be calculated through the phase-only hologram:

$$\begin{aligned} I_{mn} = &\frac{1}{PQ}\left\{\sum_{p'=-\frac{P}{2}}^{\frac{P}{2}-1}\sum_{q'=-\frac{Q}{2}}^{\frac{Q}{2}-1}\sin\left[\theta'_{p'q'} + 2\pi\left(\frac{mp'}{M}+\frac{nq'}{N}\right) - \frac{\pi p_0}{2f}z_{mn}\left(p'^2+q'^2\right)\right]\right\}^2 \\ &+\frac{1}{PQ}\left\{\sum_{p'=-\frac{P}{2}}^{\frac{P}{2}-1}\sum_{q'=-\frac{Q}{2}}^{\frac{Q}{2}-1}\cos\left[\theta'_{p'q'} + 2\pi\left(\frac{mp'}{M}+\frac{nq'}{N}\right) - \frac{\pi p_0}{2f}z_{mn}\left(p'^2+q'^2\right)\right]\right\}^2 \end{aligned} \tag{49}$$

The gradient of the intensity and the hologram is:

$$\frac{\partial I_{mn}}{\partial \theta'_{pq}} = \frac{2}{PQ}A_{mn}\sin\left[\varphi_{mn} - \theta'_{pq} - 2\pi\left(\frac{mp}{M}+\frac{nq}{N}\right) + \frac{\pi p_0}{2f}z_{mn}\left(p^2+q^2\right)\right] \tag{50}$$

Now the gradient can be calculated:

$$\frac{\partial E}{\partial \theta'_{pq}} = \frac{4}{\bar{I}MNPQ}\mathrm{Im}\left\{e^{-i\theta'_{pq}}\mathscr{T}\left[\left(\frac{I_{mn}}{\bar{I}} - \frac{I_{0-mn}}{\bar{I}_0}\right)A_{mn}e^{i\varphi_{mn}}, z_{mn}\right]\right\} \tag{51}$$

According to the principle of the gradient descent method, the phase change of each iteration can be expressed as (52).

$$\Delta\theta'_{t-pq} = -\gamma\frac{\partial E}{\partial \theta'_{pq}} \tag{52}$$

where γ is the optimization rate of each iteration.

The phase of the next iteration is shown as following.

$$\theta'_{t+1-pq} = \theta'_{t-pq} + \Delta\theta'_{t-pq} \tag{53}$$

The optimization rate can be also optimized through some method. Similar to

the research before, the optimization rate can be calculated through the estimated error of the next iteration and the gradient of this iteration.

$$E' = \frac{1}{MN} \sum_{m=-\frac{M}{2}}^{\frac{M}{2}-1} \sum_{n=-\frac{N}{2}}^{\frac{N}{2}-1} \left(\frac{I_{mn} + \Delta I_{mn}}{\overline{I}} - \frac{I_{0-mn}}{\overline{I_0}} \right)^2 \tag{54}$$

where the $\boxtimes I_{mn}$ is the estimated change of the intensity of the present iteration, which can be calculated through chain rule (55).

$$\Delta I_{mn} \approx \sum_{p=-\frac{P}{2}}^{\frac{P}{2}-1} \sum_{q=-\frac{Q}{2}}^{\frac{Q}{2}-1} \frac{\partial I_{mn}}{\partial \theta'_{pq}} \Delta \theta'_{pq} \tag{55}$$

Substitute (50) into (55).

$$\Delta I_{mn} = 2A_{mn} \mathrm{Im} e^{i\varphi_{mn}} \left[\mathscr{T} \left(\Delta \theta'_{pq} e^{i\theta'_{pq}}, z_{mn} \right) \right]^* \tag{56}$$

In order to optimize the optimization rate, γ should minimize the estimated error of the next iteration.

$$\frac{\partial E'}{\partial \gamma_0} = 0 \tag{57}$$

The calculation of the optimization rate is shown as (58).

$$\gamma_0 = - \frac{\sum_{m=-\frac{M}{2}}^{\frac{M}{2}-1} \sum_{n=-\frac{N}{2}}^{\frac{N}{2}-1} I_{mn} \cdot 2A_{mn} \mathrm{Im} e^{i\varphi_{mn}} \left\{ \mathscr{T}^{-1} \left[-\frac{\partial E}{\partial \theta'_{pq}} e^{i\theta'_{pq}}, z_{mn} \right] \right\}^*}{\sum_{m=-\frac{M}{2}}^{\frac{M}{2}-1} \sum_{n=-\frac{N}{2}}^{\frac{N}{2}-1} \left\{ 2A_{mn} \mathrm{Im} e^{i\varphi_{mn}} \left\{ \mathscr{T}^{-1} \left[-\frac{\partial E}{\partial \theta'_{pq}} e^{i\theta'_{pq}}, z_{mn} \right] \right\}^* \right\}^2} \tag{58}$$

The optimized rate calculated by the consider only the first order differential as the approximation, which the higher order differential act on the practical is ignored. To reduce the error caused by the higher order differential, we can reduce the optimization by a constant rate γ_r to reduce the error caused by higher order differential.

$$\gamma = \gamma_0 \gamma_r \tag{59}$$

In the simulations below, contrast rate γ_r is set as 0.5.

Based on the calculation of the previous, the proposed algorithm based on Gra-

dient Descent method is designed as the Fig. 23.

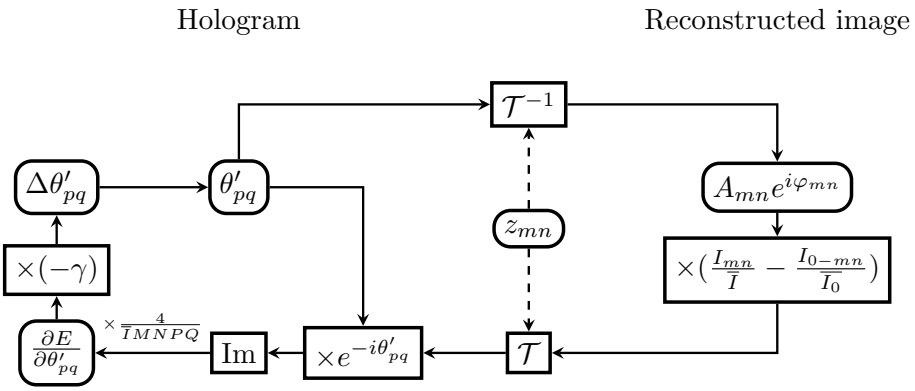

Figure 23: Flow chart of the proposed algorithm

3.4 Simulation

I test the gradient-descent based algotihm by simulation. The holograms of 1, 2, 5, 10, 50, 100 iterations are shown as Fig. 24 ("$\mathscr{LR}$" image).

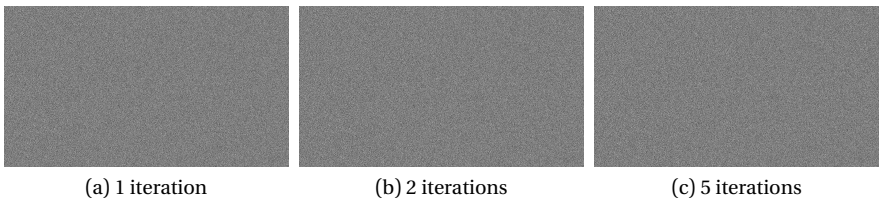

(a) 1 iteration (b) 2 iterations (c) 5 iterations

(d) 10 iterations (e) 50 iterations (f) 100 iterations

Figure 24: Holograms of 1, 2, 5, 10, 50, 100 iterations ("$\mathscr{LR}$" image)

The reconstructed images are shown as Fig. 25.

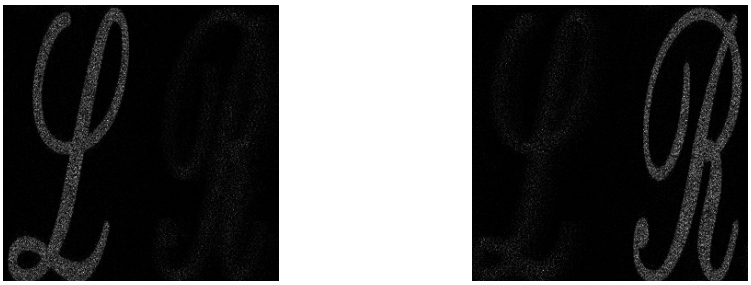

Figure 26: Reconstructed in minimum and maximum range. Left: minimum; Right: maximum

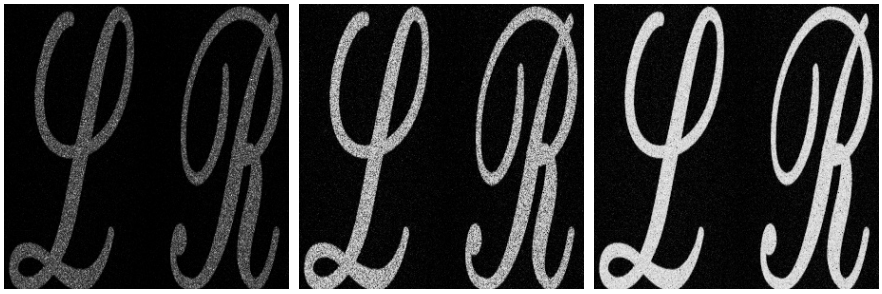

(a) 1 iteration (b) 2 iterations (c) 5 iterations

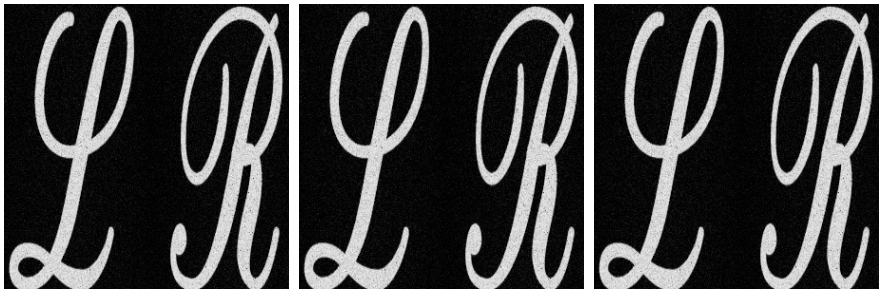

(d) 10 iterations (e) 50 iterations (f) 100 iterations

Figure 25: Reconstructed images of 1, 2, 5, 10, 50, 100 iterations ("$\mathscr{LR}$" image)

We reconstruct from the hologram of 100 iterations with the depth option of minimum range and maximum range to show the reconstructed images of different planes as Fig. 26.

The grid image was also set as the target image in simulation. The holograms and the reconstructed images are shown as Fig. 27 and Fig. 28.

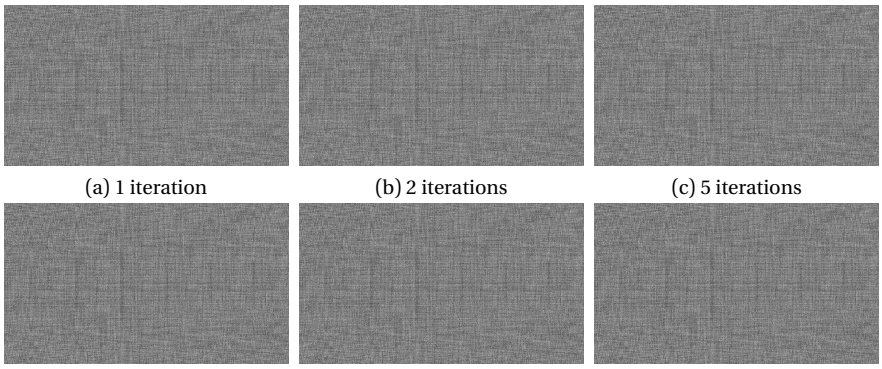

(a) 1 iteration (b) 2 iterations (c) 5 iterations

(d) 10 iterations (e) 50 iterations (f) 100 iterations

Figure 27: Holograms of 1, 2, 5, 10, 50, 100 iterations (”grid” image)

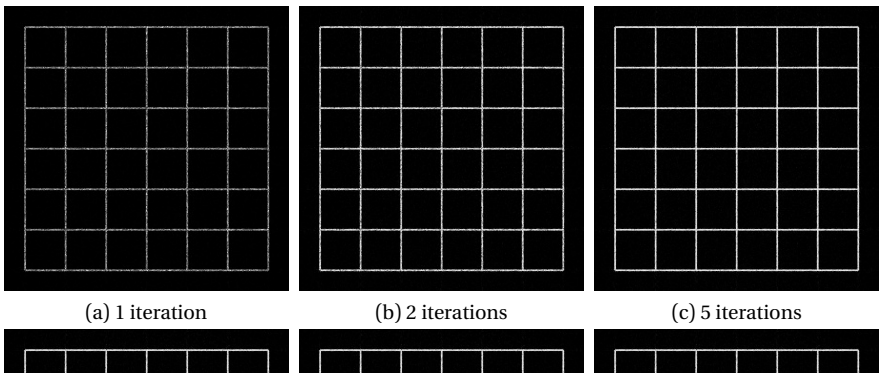

(a) 1 iteration (b) 2 iterations (c) 5 iterations

(d) 10 iterations (e) 50 iterations (f) 100 iterations

Figure 28: Reconstructed images of 1, 2, 5, 10, 50, 100 iterations (“grid” image)

The MSE-iteration graph is shown as Fig. 29.

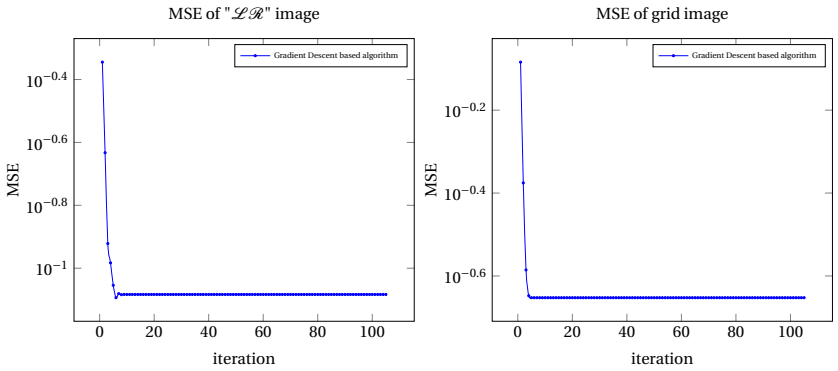

Figure 29: MSE-iteration graphs

We know that the MSE convergences after about 15 iterations. The MSE reaches the local minimum and no longer changes after convergence.

3.5 Experimental Results

We did experiments to verify the correctness of the proposed algorithm. The optical system was set as the Fig. 30 shows.

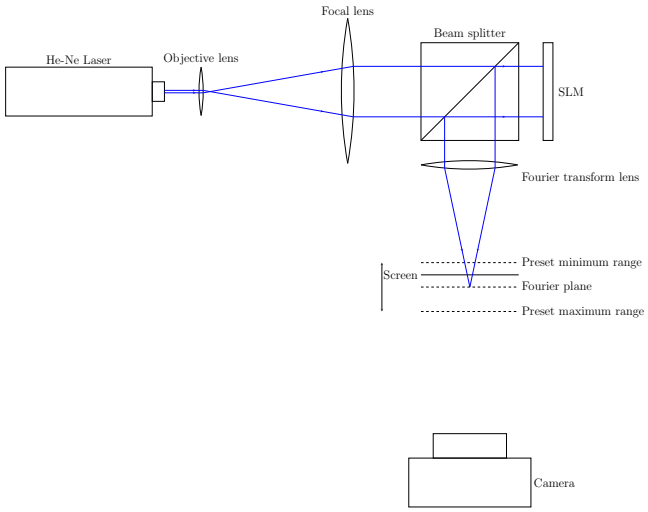

Figure 30: Optical system

In the experiments of the "$\mathscr{LR}$" image, the screen was set in different depth position from the Fourier transform lens. As the Fig. 17 shows, the letter "$\mathscr{L}$" was set on the plane in the preset minimum range, and the letter "$\mathscr{R}$" was set on the plane in the preset maximum range. To take the clear letter "$\mathscr{L}$", we first set the

screen at the preset minimum range. The result of the reconstructed images by the holograms produced by Gradient Descent based algorithm and modified GS algorithm are shown as Fig. 31.

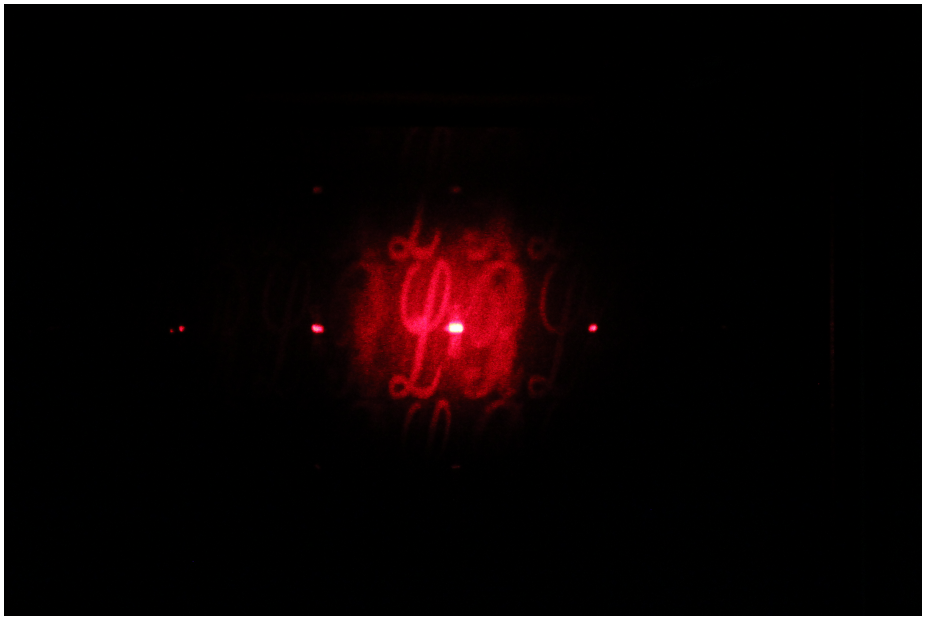

Figure 31: Reconstructed letter "$\mathscr{L}$".

As we take the clear letter "$\mathscr{L}$", the letter "$\mathscr{R}$" blurred because the letter "$\mathscr{R}$" is in another plane. To take the clear letter "$\mathscr{R}$", the screen was set at the preset maximum range. The result of the letter "$\mathscr{R}$" is shown as Fig. 32.

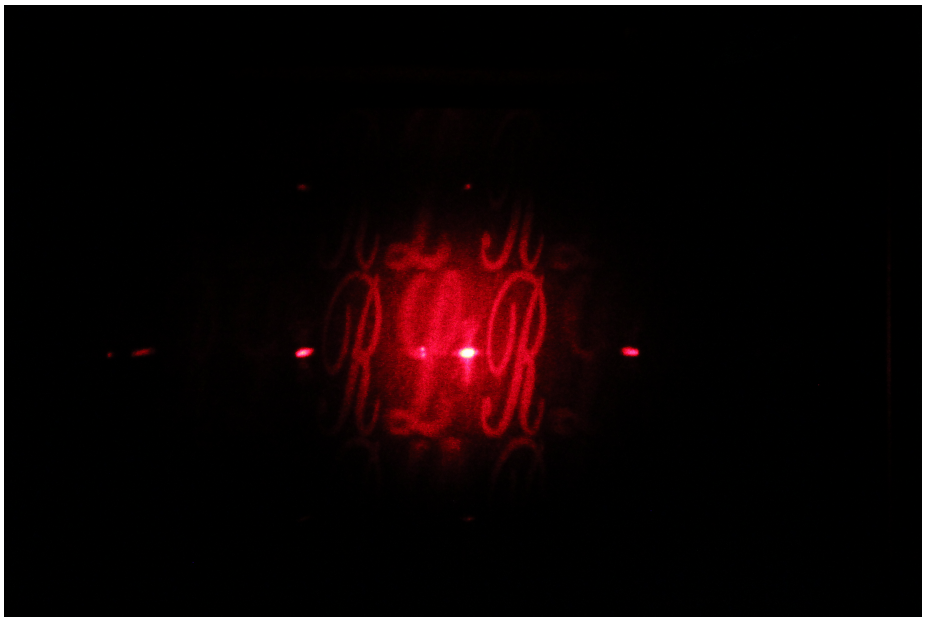

Figure 32: Reconstructed letter "$\mathscr{R}$".

The results of "$\mathscr{LR}$" image shows that both Gradient Descent based algorithm and modified GS algorithm can produce holograms that able to reconstruct images clear enough.

In the experiments of the grid image, we set a tilted screen as the Fig. 18 shows. The results of "grid" image produced by two algorithms are shown as Fig. 33.

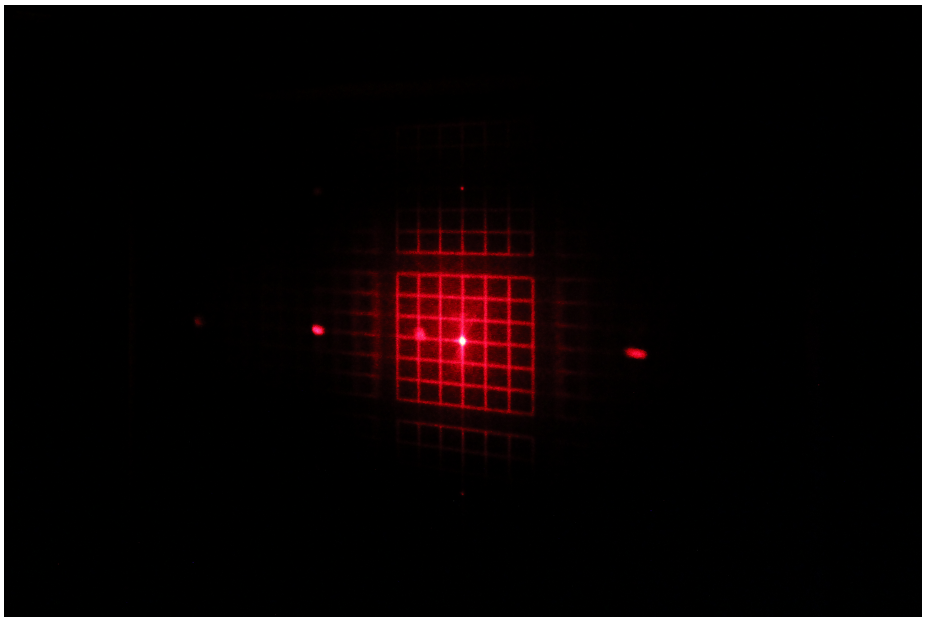

Figure 33: Reconstructed “grid” images.

The proposed algorithm shows correctness on reconstructing the grid image in an inclined screen. The image correctly reconstructed on the expected plane. The algirithm also possess the ability to regenerate images on irregular screen, however, the irregular screen is hard to practice in experiment with such optical system.

3.6 Discussion

A Fresnel transform with the utilization of a Fourier transform lens was proposed. The transform succeeded in generating holograms of 3D images. Moreover, based on the transform, a Gradient Descent based algorithm for phase-only computer-generated holograms was proposed, which shows a high effectiveness.

4 Comparison of Optimization Schemes

4.1 Optimization Schemes

Gradient-descent algorithm, first developed by Cauchy in 1847, is a first order iterative optimization algorithm. Gradient-descent based algorithms are developed rapidly with the development of Machine-Learning, especially in the field of Deep-Learning.

The utilization on Deep-Learning stimulates the development of optimizatin schemes based on gradient-descent algorithm. These optimization schemes include momentum, adagrad, RMSprop, Adadelta, Adam etc.. Here we compare these algorithms with the method mentioned in section 2.2.2. All the algorithms mentioned before shows a high efficiency in the task of Deep-Learning. They may also show a higher efficiency in the task of phase-only CGH.

4.1.1 Momentum

Momentum is a method that accelerates the Batch gradient descent when the relevant direction and dampens oscillations. When sthe gradient oscillation, the naive batch gradient descent algorithm become slow and unstable. As the Fig. 34 shows, the naive batch gradient descent algorithm become slow in such scenario.

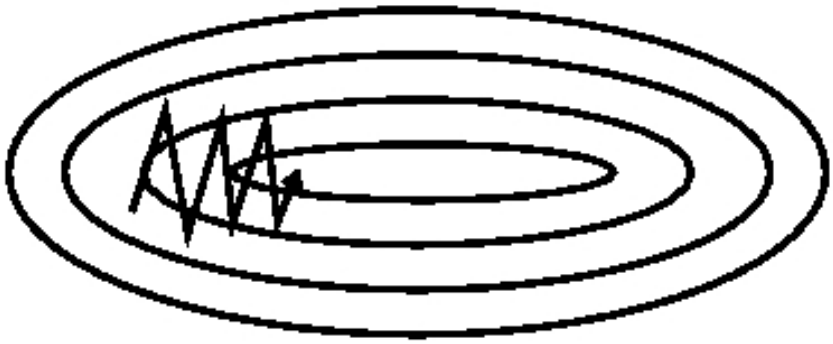

Figure 34: Naive batch gradient descent algorithm

Contrary to such scenario, the momentum method was developed. In the field of naive batch gradient descent algorithm, the increment of the independent variable is the gradient times optimization rate.

$$\Delta\theta_t = -\eta \frac{\partial E(\theta_t)}{\partial \theta_t} \tag{60}$$

where η is the optimization rate, which is usually a constant number. E stand for the error function. t stand for the current iteration number.

The momentum method add the history information to the increment each iteration. The function of the increment is shown as below.

$$\begin{aligned} v_t &= \gamma v_{t-1} + \eta \frac{\partial E(\theta_t)}{\partial \theta_t} \\ \Delta\theta_t &= -v_t \end{aligned} \tag{61}$$

where γ discribes the inertia of the history information, which is usually set to 0.9. v_t determines the increment of the iteration.

Momentum method can reduce strong oscillations of the error function, and increase the unified part. The simulation result of the momentum in the scenario mentioned formerly is shown as Fig. 35.

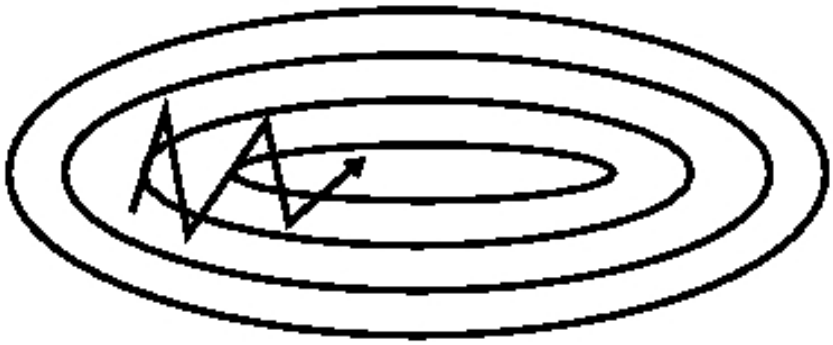

Figure 35: Momentum algorithm

This example shows that the momentum algorithm accelerates the optimization in the scenario that the gradient oscillation in some dimention. Such scenario may occur in the task of phase-only CGH. If so, the momentum algorithm may gring a higher efficiency than naive batch gradient descent algorithm.

4.1.2 Nesterov accelerated gradient

Nesterov acclerated gradient (NAG) algorithm is an algorithm based on momentum, which gives ability to prescience. The algorithm of each iteration of NAG is shown as below:

$$\begin{aligned} v_t &= \gamma v_{t-1} + \eta \frac{\partial E(\theta_t - \gamma v_{t-1})}{\partial \theta_t} \\ \Delta\theta_t &= -v_t \end{aligned} \tag{62}$$

This algorithm provides a prescision ability that may speed up the iteration somehow. Comparing with the momentum algorithm, NAG algorithm can speed up in some special scenario, however, not all scenarios fit the NAG.

Similarl to the momentum algorithm, the optimization rate η is set to 0.9 in this research.

4.1.3 Adagrad

Adagrad is a gradient-descent based algorithm that widely utilized in the field of sparse features. The desired feature is decreasing the learning rate while training. This feature is fit for language models.

Adagrad algorithm adapt the optimization rate for every features, the optimization rate become lower for the frequent feature. For the infrequent feature, the optimization is high. Thus, for phase-only CGH calculation, this algorithm may produce a high performance in a few times at beginning, and produce a stable result as the iteration increases.

The batch gradient descent treat every independent variable with a same pattern (63).

$$\theta_{t+1,i} = \theta_{t,i} - \eta \frac{\partial E(\theta_{t,i})}{\partial \theta_i} \tag{63}$$

where i is the coordination of independent variable θ. η is the optimization rate.

Adagrad algorithm does not adopt a universe optimization rate for every coordinate. The η is replaced by η_i. For each coordinate, the optimization function is shown as below.

$$
\begin{aligned}
g_{t,i} &= \frac{\partial E(\theta_{t,i})}{\partial \theta_i} \\
s_{t,i} &= s_{t-1,i} + g_{t,i}^2 \\
\eta_i &= \frac{\eta}{\sqrt{s_{t,i} + \epsilon}} \\
\theta_{t+1,i} &= \theta_{t,i} - \eta_i g_{t,i}
\end{aligned}
\tag{64}
$$

where s_t is an adapted parameter for each coordinate and for all the coordinate i, $s_{0,i}$ are initialized as 0. ϵ is a small number to prevent the $s_{t,i}$ to be too small and make the η_i too big. $g_{i,i}$ is the gradient of each coordinate. η is the main learning rate that usually preset as 0.05.

The equation (64) is the equation of each coordinate of the independent variable. The integral form of the Adagrad algorithm is shown as (65)

$$
\begin{aligned}
g_t &= \frac{\partial E(\theta_t)}{\partial \theta} \\
s_t &= s_{t-1} + g_t \odot g_t \\
\theta_{t+1} &= \theta_t - \frac{\eta}{\sqrt{s_t + \epsilon}} \odot g_t
\end{aligned}
\tag{65}
$$

From the equation, we can know that the s_t become bigger and bigger while the iteration continuing. Thus, the optimization rate become smaller and smaller. The result become stable with the iteration continues. The main disadvantage is that the algorithm would not accept new knowledge after several iterations. This may get solved by the following algorithms.

4.1.4 RMSprop

Aiming at the disadvantages of Adagrad algorithm, RMSprop are developed to solve the problem. The RMSprop algorithm merges the momentum algorithm and Adagrad algorithm to reduce the disadvantage of Adagrad algorithm.

As the method of momentum, RMSprop adapt the s_t as following.

$$
s_t = \gamma s_{t-1} + (1-\gamma) g_t \odot g_t \tag{66}
$$

where γ is a rate of the parameter s_t updating, which is suggested to set around 0.9.

The update of s_t changes with momentum method, and the iteration updating function is the same with Adagrad.

$$\theta_{t+1} = \theta_t - \frac{\eta}{\sqrt{s_t + \epsilon}} \odot g_t \tag{67}$$

where η is the optimization rate, same with Adagrad. ϵ is the number to avoid the result of the s_t to be too small.

This algorithm changes the s_t updating algorithm of the Adagrad algorithm. The s_t does not become bigger and bigger and eventually does not change when the new knowledge inputs. The optimization rate still strongly related to the history. In the cast of phase-only CGH, this may bring a stability of a certain coordinate, increment of a certain coorinate should not be too big. The increment over 2π is pointless in phase.

4.1.5 Adadelta

Adadelta is another algorithm for solving the disadvantages of Adagrad, and independently developed with the RMSprop. Adadelta updates another parameter $\Delta\theta_t$ to determine the optimization rate.

Similarly, the Adadelta update the parameter s_t same with the RMSprop algorithm.

The flow of the Adadelta algorithm is shown as following.

$$s_t = \rho s_{t-1} + (1-\rho) g_t \odot g_t \tag{68}$$

where ρ is the changing rate of the s_t, same with γ in RMSprop, which usually set around 0.9.

$$g'_t = \sqrt{\frac{\Delta\theta_{t-1} + \epsilon}{s_t + \epsilon}} \odot g_t \tag{69}$$

where $\Delta\theta_{t-1}$ is the leaky average of the squared rescaled gradients g'_t.

Then update the independent variant.

$$\theta_t = \theta_{t-1} - g'_t \tag{70}$$

At last, update the $\Delta\theta_t$

$$\Delta\theta_t = \rho\Delta\theta_{t-1} + (1-\rho)g'_t \odot g'_t \tag{71}$$

The main difference between RMSproop and Adadelta is replacing the constant parameter η with the updated parameter $\sqrt{\Delta\theta_{t-1}}$. Adadelta may improve the efficient from RMSprop algorithm in phase-only CGH task, because the optimization rate floats through the history and bring a reasonable optimization rate when some coordinate of the phase is too big.

4.1.6 Adam

Adam is the almost the "ultimate" algorithm for Deep-Learning. Merged with many algorithms, adam show a very high efficient in many tasks. The flow of the algorithm is shown as following.

Adam algorithm updates 2 momentum variable. Same with the momentum algorithm, an adapted v_t is updated.

$$v_t = \beta_1 v_{t-1} + (1-\beta_1)g_t \tag{72}$$

where β_1 is a preset constant parameter for updating v_t

There is also a counter part of RMSprop, the momentum parameter s_t is updated as follows.

$$s_t = \beta_2 s_{t-1} + (1-\beta_2)g_t \odot g_t \tag{73}$$

where $beta_2$ is also a preset constant parameter for updating s_t

Correspondingly the normalized state variables are given by 74.

$$\begin{aligned} \hat{v}_t &= \frac{v_t}{1-\beta_1^t} \\ \hat{s}_t &= \frac{s_t}{1-\beta_2^t} \end{aligned} \tag{74}$$

The increment is calculated by 75.

$$g'_t = \frac{\eta\hat{v}_t}{\sqrt{\hat{s}_t}+\epsilon} \tag{75}$$

Update the independent variable with increment.

$$\theta_t = \theta_{t-1} - g'_t \tag{76}$$

Adam algorithm show a very high efficient in the task of Deep-Learning. Adam may also show a high efficiency in the task of phase-only CGH.

4.2 Simulations

A comparison is made through generating holograms of "mandrill" with different methods. 8 algorithms, including naive batch gradient descent, batch gradient descent with dynamic optimization rate mentioned in section 2.2.2, momentum, Nesterov accelerated gradient, Adagrad, Adadelta, RMSprop and Adam, are adopted to participate in the comparison.

The test image is Mandrill with the resolution of 512×512 with a uniformed initial random phase. The simulation of naive batch gradient descent algorithm and proposed method has done in section 2.3. Here the simulation of 6 optimization scemes are made. All the simulation are made in 2D image.

4.2.1 Momentum

In the simulation of momentum, the optimization rate was set to 0.05 and the momentum parameter was set to 0.9. The hologram and regenerated image of 1, 2, 5, 10, 50, 100 iteration are shown as Figs. 36 and 37.

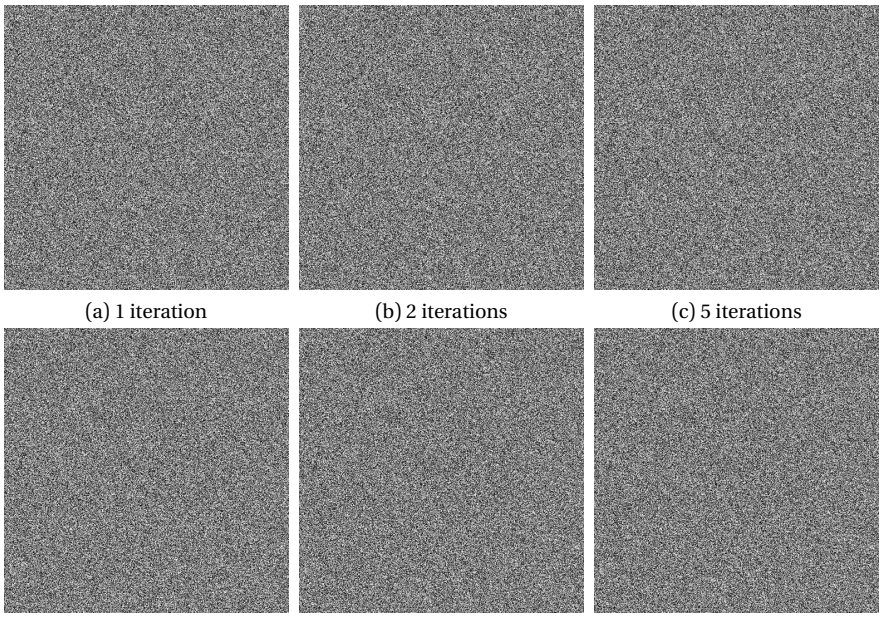

(a) 1 iteration (b) 2 iterations (c) 5 iterations

(d) 10 iterations (e) 50 iterations (f) 100 iterations

Figure 36: Generated holograms of 1, 2, 5, 10, 50, 100 iterations

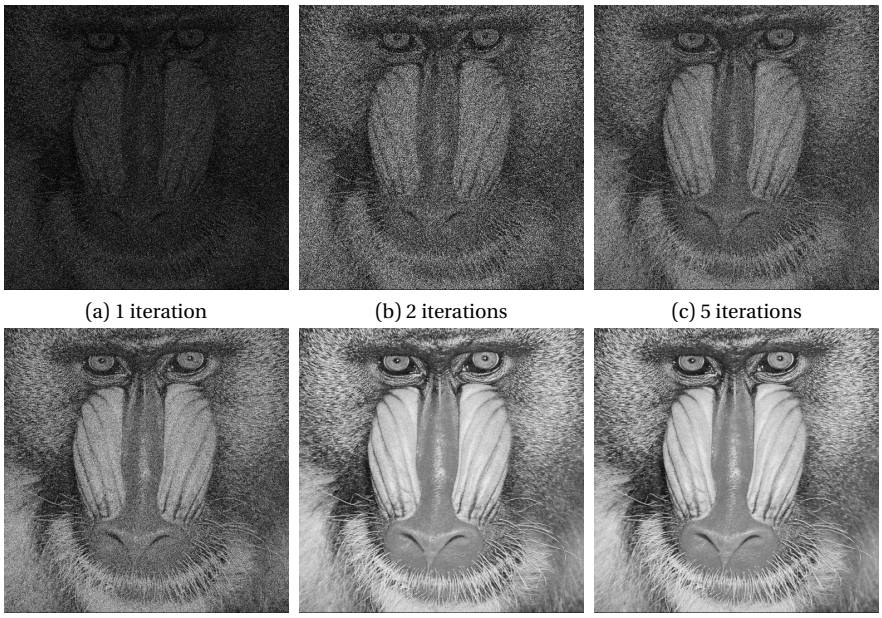

(a) 1 iteration (b) 2 iterations (c) 5 iterations

(d) 10 iterations (e) 50 iterations (f) 100 iterations

Figure 37: Regenerated images of 1, 2, 5, 10, 50, 100 iterations

The MSE-iteration graph is shown as Fig. 38.

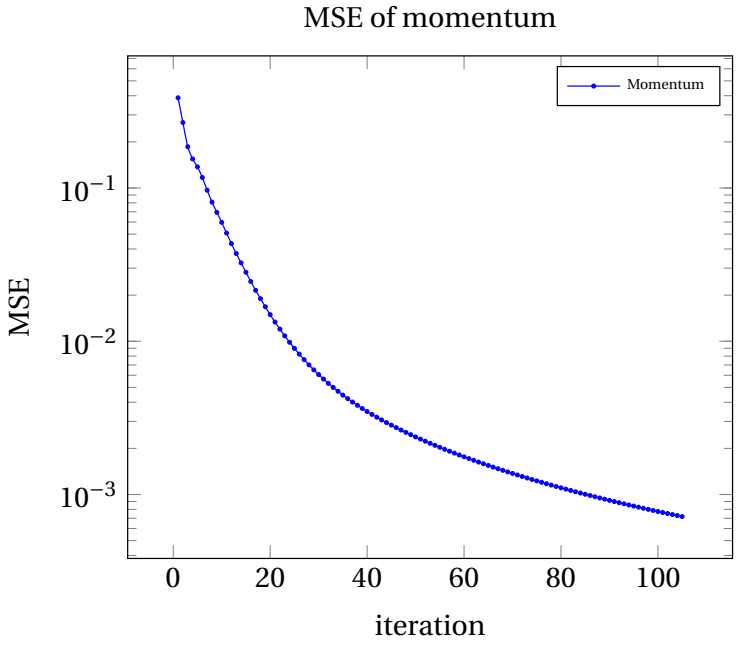

Figure 38: MSE-iteration graph of momentum algorithm

Through the MSE-iteration relation, we can see that the MSE does not reach the convergence after 100 iterations. The MSE may decrease continuously if the iteration continues.

4.2.2 Nesterov Accelerated Gradient

NAG algorithm is somehow similar with momentum algorithm, the optimization rate is set to 0.05 and the momentum parameter is set to 0.9. The hologram and regenerated image of 1, 2, 5, 10, 50, 100 iteration are shown as Figs. 39 and 40.

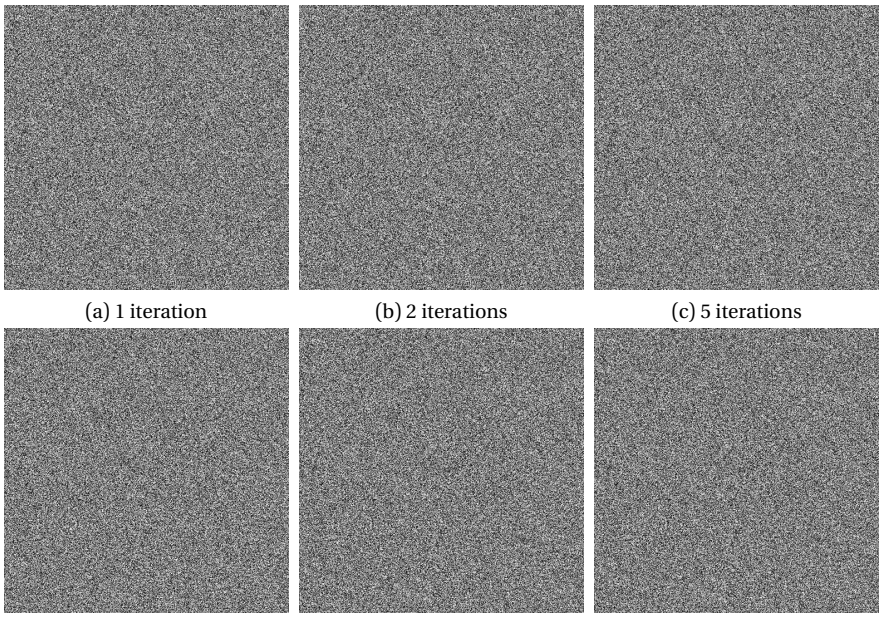

(a) 1 iteration (b) 2 iterations (c) 5 iterations

(d) 10 iterations (e) 50 iterations (f) 100 iterations

Figure 39: Generated holograms of 1, 2, 5, 10, 50, 100 iterations

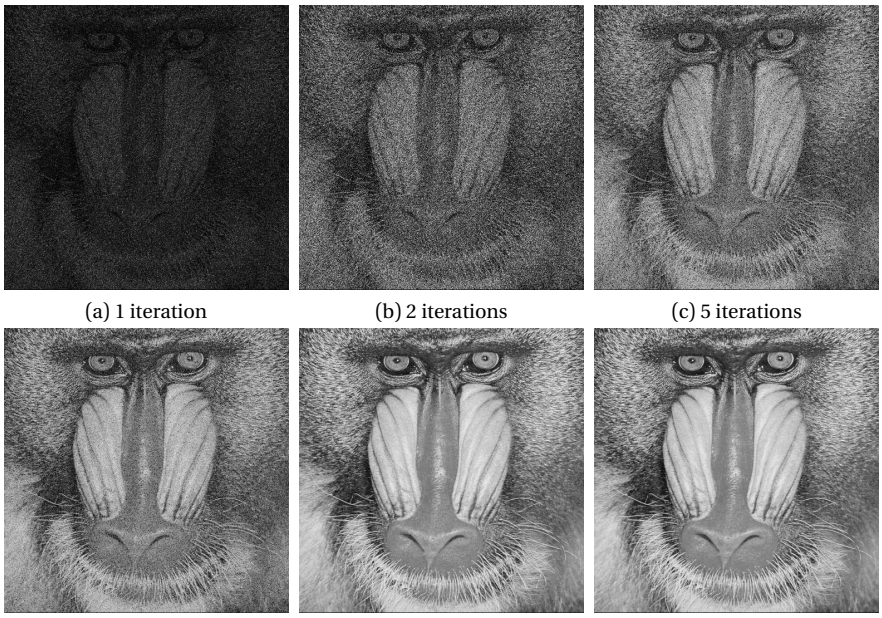

(a) 1 iteration (b) 2 iterations (c) 5 iterations

(d) 10 iterations (e) 50 iterations (f) 100 iterations

Figure 40: Generated images of 1, 2, 5, 10, 50, 100 iterations

The MSE-iteration graph is shown as Fig. 41.

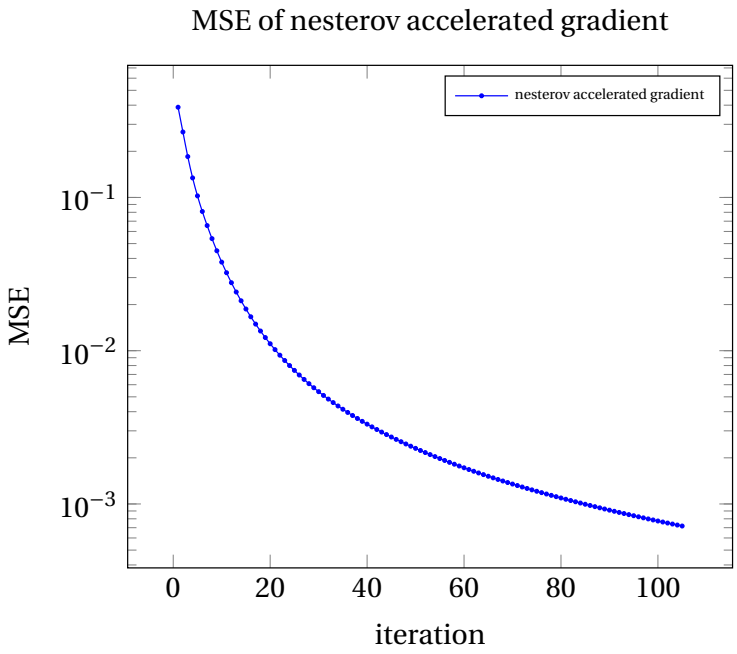

Figure 41: MSE-iteration graph of NAG algorithm

The NAG algorithm is a momentum-based algorithm with optimization, thus, the shape of the MSE-iteration graph is similar. NAG algorithm does not reach the convergence after 100 iterations as well.

4.2.3 Adagrad

The simulation of Adagrad algorithm was made with the optimization rate (η) of 0.0025. The result is strongly related with the optimization rate, for example, the optimization rate of 0.05 bring a very bad result which the MSE increases during iteration. All the small numbers ϵ was set to 10^{-6} in Adagrad, RMSprop, Adadelta and Adam algorithms. The hologram and regenerated image of 1, 2, 5, 10, 50, 100 iteration are shown as Figs. 42 and 43.

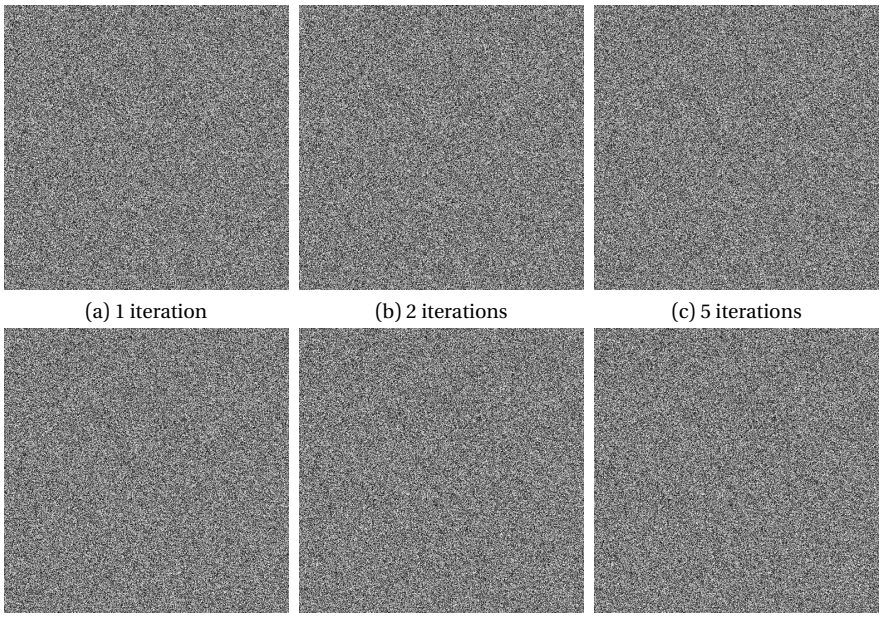

(a) 1 iteration (b) 2 iterations (c) 5 iterations

(d) 10 iterations (e) 50 iterations (f) 100 iterations

Figure 42: Generated holograms of 1, 2, 5, 10, 50, 100 iterations

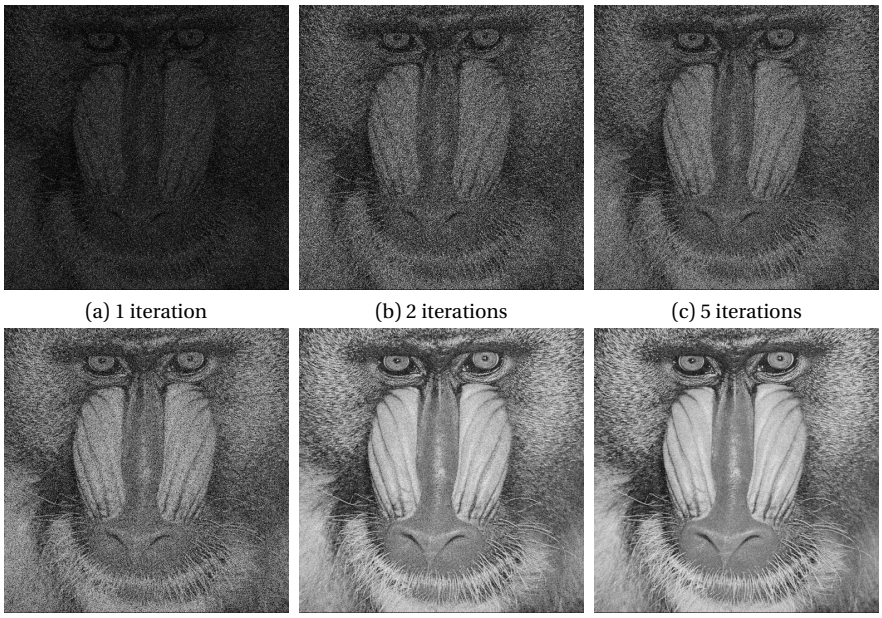

(a) 1 iteration (b) 2 iterations (c) 5 iterations

(d) 10 iterations (e) 50 iterations (f) 100 iterations

Figure 43: Generated images of 1, 2, 5, 10, 50, 100 iterations

The MSE-iteration graph is shown as Fig. 44.

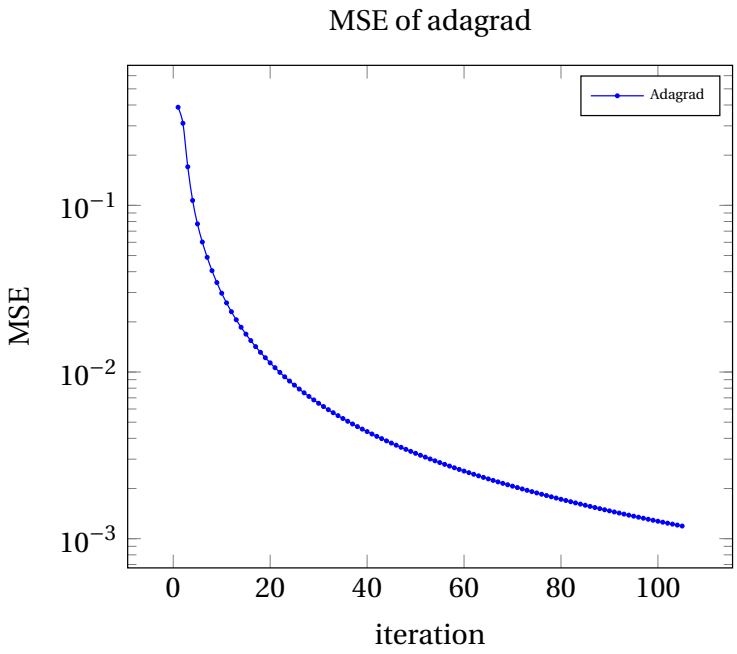

Figure 44: MSE-iteration graph of Adagrad algorithm

4.2.4 RMSprop

RMSprop algorithm also requires an optimization rate (η). The optimization rate is set as 0.0025 as well. The robustness of RMSprop is far smaller than the Adagrad. If the optimization was set to 0.01, the MSE increases during the iteration. The momentum parameter γ is set to 0.9. The hologram and regenerated image of 1, 2, 5, 10, 50, 100 iteration are shown as Figs. 45 and 46.

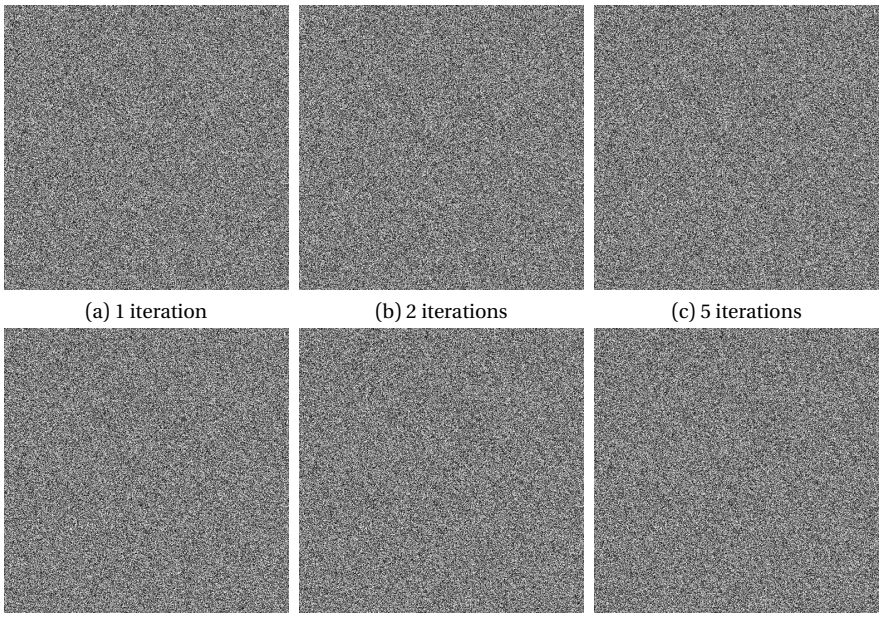

(a) 1 iteration (b) 2 iterations (c) 5 iterations

(d) 10 iterations (e) 50 iterations (f) 100 iterations

Figure 45: Generated holograms of 1, 2, 5, 10, 50, 100 iterations

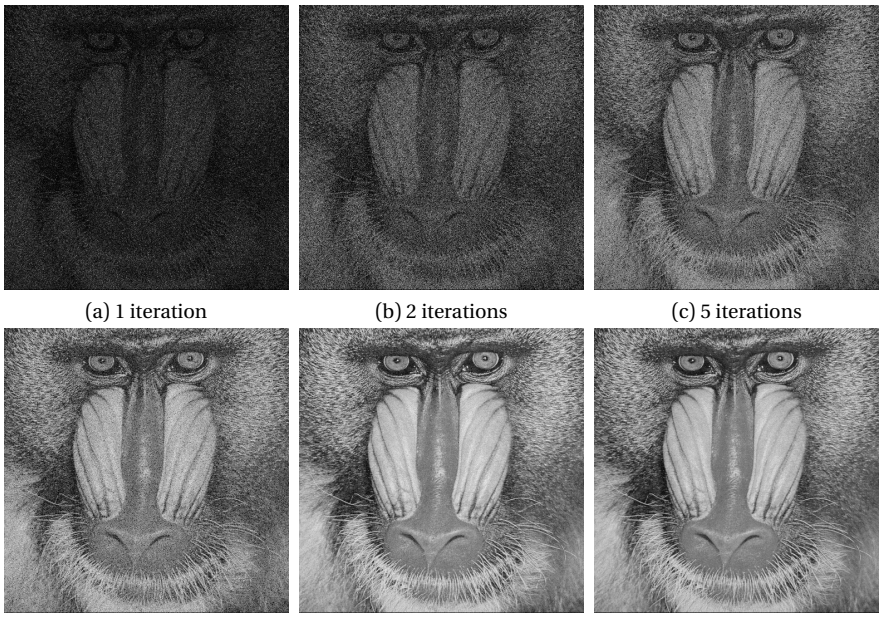

(a) 1 iteration (b) 2 iterations (c) 5 iterations

(d) 10 iterations (e) 50 iterations (f) 100 iterations

Figure 46: Generated images of 1, 2, 5, 10, 50, 100 iterations

The MSE-iteration graph is shown as Fig. 47.

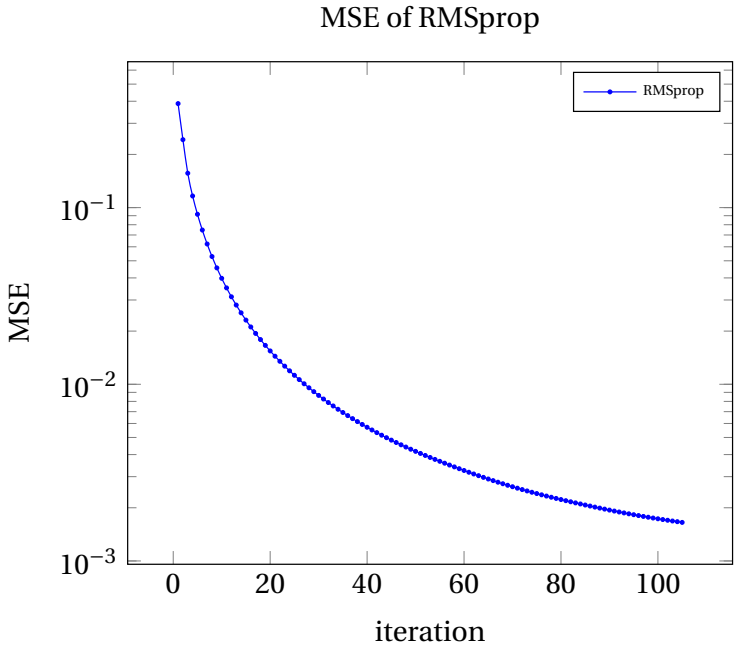

Figure 47: MSE-iteration graph of RMSprop algorithm

4.2.5 Adadelta

Adadelta also require a parameter for updating s_t, the parameter ρ is set to 0.9 as well. The hologram and regenerated image of 1, 2, 5, 10, 50, 100 iteration are shown as Figs. 48 and 49.

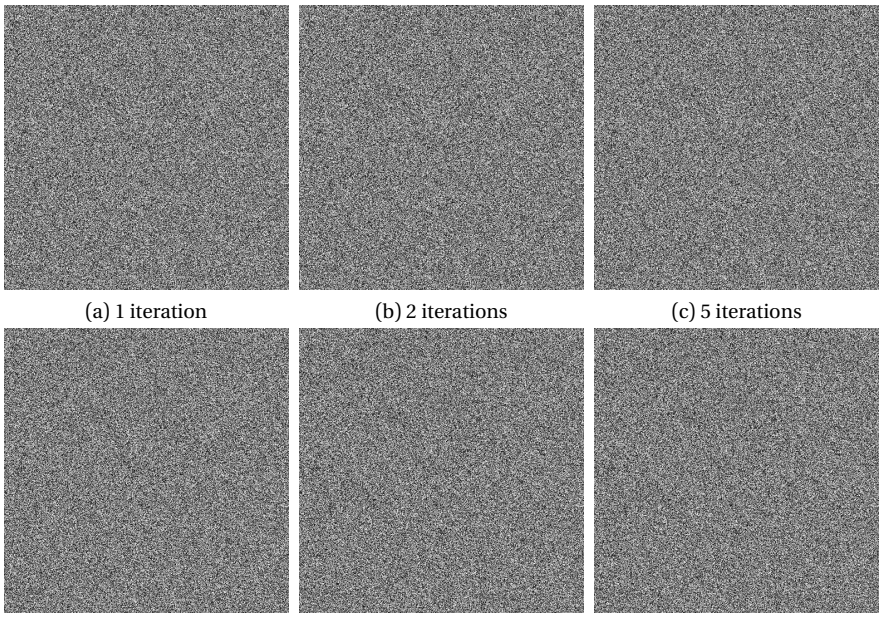

(a) 1 iteration (b) 2 iterations (c) 5 iterations

(d) 10 iterations (e) 50 iterations (f) 100 iterations

Figure 48: Generated holograms of 1, 2, 5, 10, 50, 100 iterations

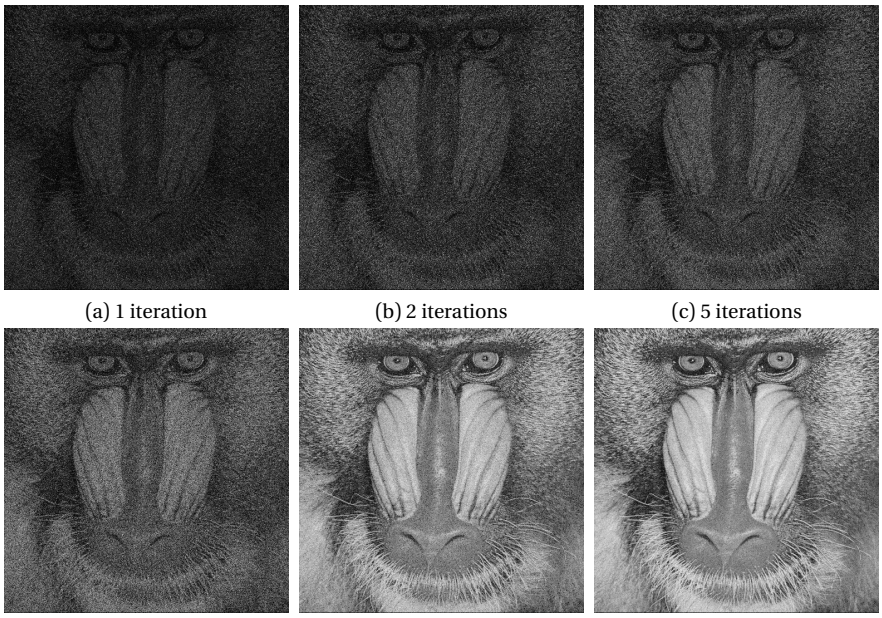

(a) 1 iteration (b) 2 iterations (c) 5 iterations

(d) 10 iterations (e) 50 iterations (f) 100 iterations

Figure 49: Generated images of 1, 2, 5, 10, 50, 100 iterations

The MSE-iteration graph is shown as Fig. 50.

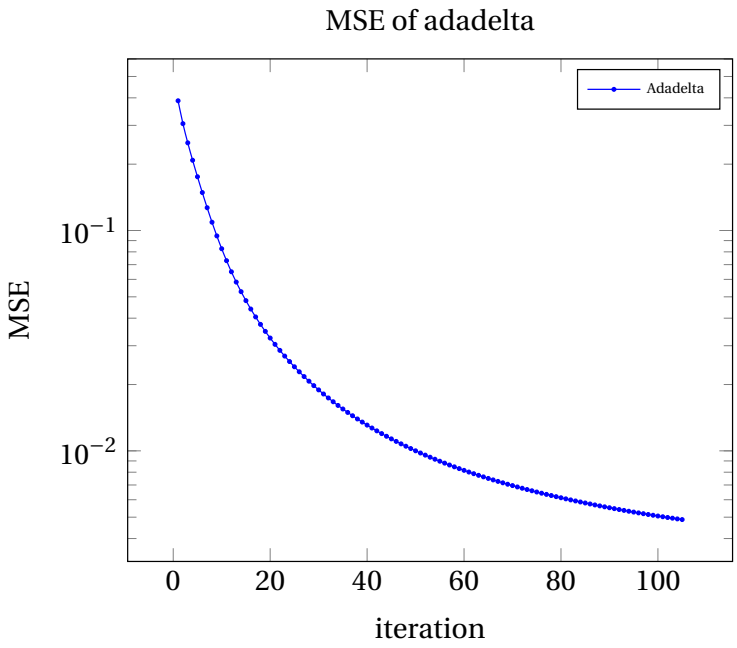

Figure 50: MSE-iteration graph of Adadelta algorithm

4.2.6 Adam

Adam requires 3 parameters (β_1, β_2, η). In this simulation, β_1 and β_2 is set as 0.85, and the optimization rate η is set to 0.1. The hologram and regenerated image of 1, 2, 5, 10, 50, 100 iteration are shown as Figs. 51 and 52.

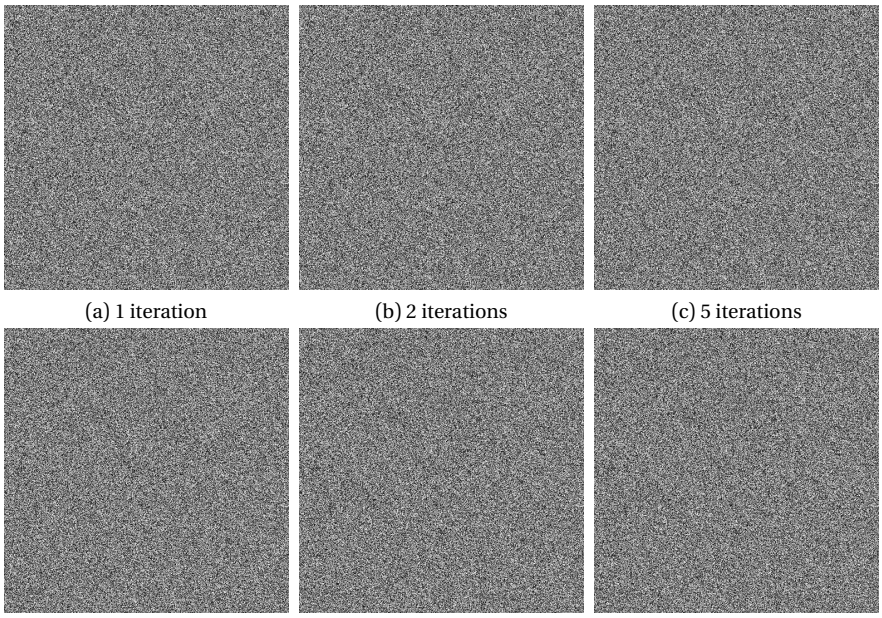

(a) 1 iteration (b) 2 iterations (c) 5 iterations

(d) 10 iterations (e) 50 iterations (f) 100 iterations

Figure 51: Generated holograms of 1, 2, 5, 10, 50, 100 iterations

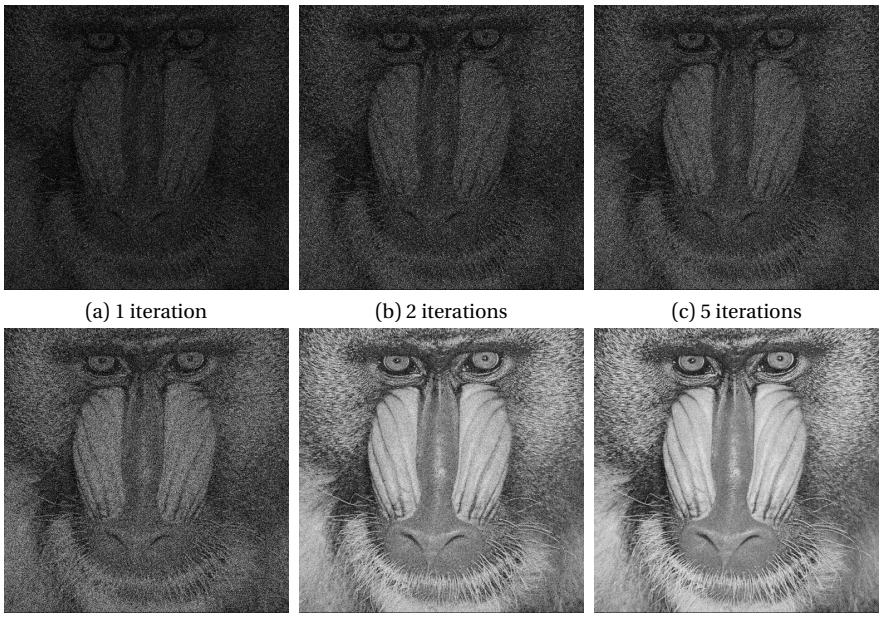

(a) 1 iteration (b) 2 iterations (c) 5 iterations

(d) 10 iterations (e) 50 iterations (f) 100 iterations

Figure 52: Generated images of 1, 2, 5, 10, 50, 100 iterations

The MSE-iteration graph is shown as Fig. 53.

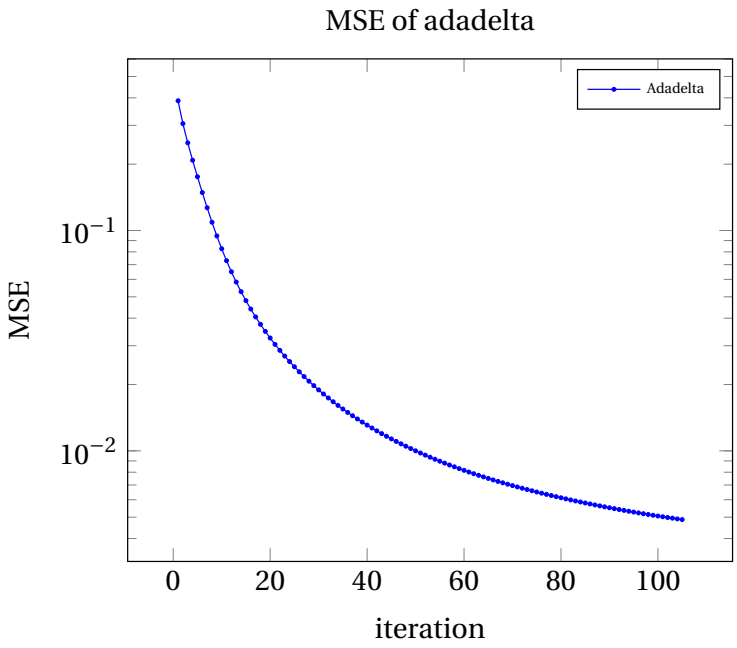

Figure 53: MSE-iteration graph of Adam algorithm

4.2.7 Comparison

To make a comparison, all the regenerated images and holograms of 100 iterations are put together as Figs. 54 and 55

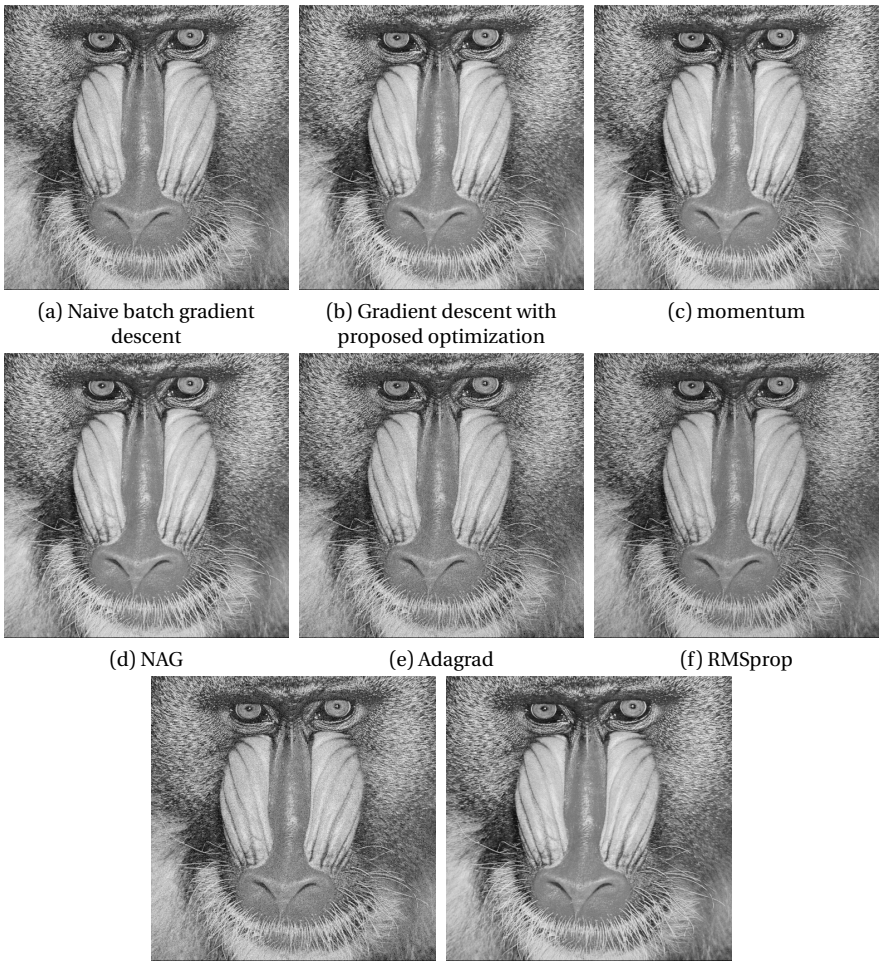

(a) Naive batch gradient descent

(b) Gradient descent with proposed optimization

(c) momentum

(d) NAG

(e) Adagrad

(f) RMSprop

(g) Adadelta

(h) Adam

Figure 54: Generated images of 100 iterations of different optimization schemes

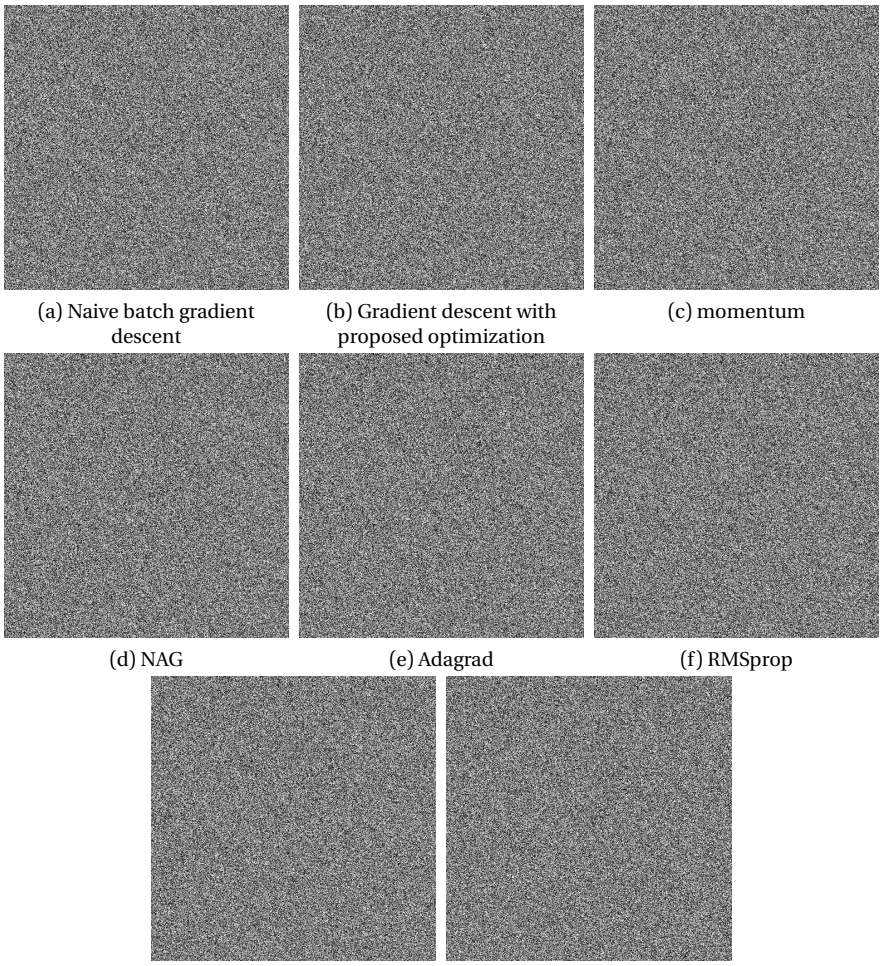

(a) Naive batch gradient descent
(b) Gradient descent with proposed optimization
(c) momentum
(d) NAG
(e) Adagrad
(f) RMSprop
(g) Adadelta
(h) Adam

Figure 55: Generated images of 100 iterations of different optimization schemes

I put MSE-iteration curves of all optimization scemes in a single graph (Fig. 56)

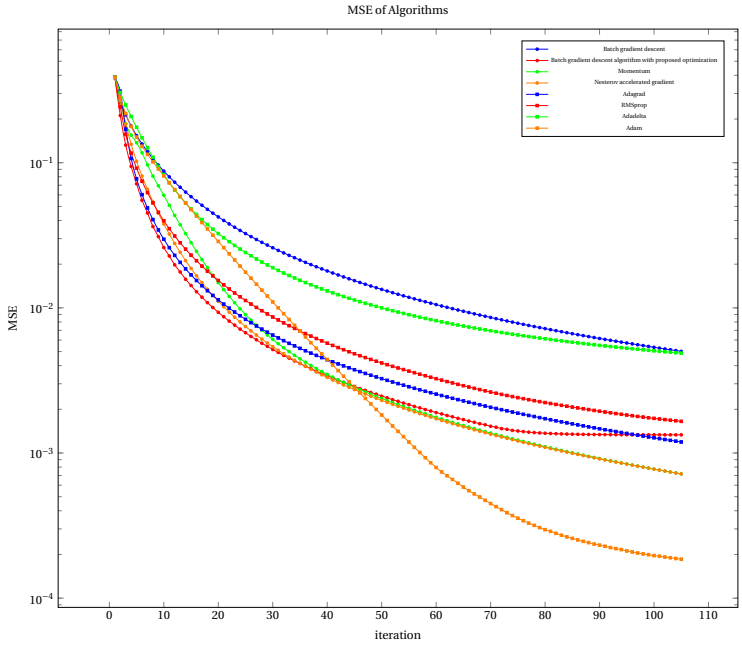

Figure 56: MSE-iteration curves

4.3 Discussion

With the development of Deep-Learning recent years, the gradient-descent based optimization schemes get faster and faster. After the Adam algorithm, new optimization schemes were developed such as Nadam, AdaMAx and RMSgrad. However, new algorithms are not get tested sufficiently.

The Fig. 56 shows that the Adam algorithm reaches the lowest error in 100 iterations, however, Adam algorithm does not stay on the lowest error in all time. The proposed optimization keep the lowest error in the starting 30 iterations, however, slow down the speed significantly after 70 iterations. Naive batch gradient descent algorithm is the slowest one, but the MSE reaches an acceptable value (0.01) in 100 iterations. Momentum and NAG algorithm are similar, and the results are similar as well. Adagrad algorithm and heritors, RMSprop and Adadelta, are similar in shape, however, the heritors does not cover the Adagrad algorithm in the task of phase-only CGH.

In this comparison, the first one to get the error of 0.01 is the proposed optimization. The algorithm which reach the lowest error is Adam.

5 Fresnel Transform with the Utilization of Fourier Lens (FrTFL) and Applications

A transform for generating holograms of 3D images are developed in section 3. This Fresnel transform with the utilization of Fourier lens brings new capability in many aspects that rely on the Fourier transform or the Fresnel transform.

The FrTFL is similar to the Fractional Fourier transform (FRFT). Some softwares that rely on the Fourier transform upgrade themselves by replacing the Fourier transform by the FRFT. Image compression algorithm with the utilization of the FRFT can simutaneously encrypt images. Blind watermarking software can also replace the Fourier transform with the FRFT and encrypt the watermark.

In this section, I discuss the same and difference of the FRFT and FrTFL. The image encryption, compression and watermarking algorithm would be discussed as well. Algorithms for image encryption, compression and watermarking with FrTFL would be designed

5.1 Comparison of Fractional Fourier Transform (FRFT) and FrTFL

In the field of image encryption, Fractional Fourier transform are usually adopted to encrypt images.

Consider about the n-iterated Fourier transform.

$$\mathscr{F}^n[f] = \mathscr{F}[\mathscr{F}^{n-1}[f]] \tag{77}$$

The sequence is finite since $\mathscr{F}$ is a 4-periodic automorphism, that satisfied with (78)

$$\mathscr{F}^4[f] = \mathscr{F}^0[f] = f \tag{78}$$

The FRFT provides a family of linear transforms that further extends this definition to handle non-integer powers $n = \frac{2\alpha}{\pi}$ of the Fourier transform.

The FRFT was defined as follows. For any real α, the α-angle fractional Fourier transform of a function is denoted by $\mathscr{F}_\alpha(u)$ and defined by

$$\mathscr{F}_\alpha(u) = \sqrt{1 - i\cot(\alpha)}\, e^{i\pi\cot(\alpha)u^2} \int_{-\infty}^{+\infty} e^{-i2\pi\left[\csc(\alpha)ux - \frac{\cot(\alpha)}{2}x^2\right]} f(x)dx \tag{79}$$

Formally, this formula is only valid when the input function is in a sufficiently nice space.

This translate possess many features like complex number.

$$\mathscr{F}_{\alpha+\beta} = \mathscr{F}_{\alpha} \circ \mathscr{F}_{\beta} = \mathscr{F}_{\beta} \circ \mathscr{F}_{\alpha} \tag{80}$$

Considering the parts of the FRFT and the FrTFL, there are 2 common parts, that is plane wave and spherical wave. Thus, the Fourier lens always do the FRFT even object and screen are not put on the Fourier plane.

5.2 Image Encryption using FrTFL

Many image encryption algorithm is using the FRFT. A simple encryption algorithm's fundamental principle is that do the FRFT with a certain order α. This make the encryped image unreadable. The decryption method is doing the FRFT with order $-\alpha$. The principle is mentioned formerly.

$$\mathscr{F}_{\alpha} \circ \mathscr{F}_{-\alpha} = \mathscr{F}_{\alpha-\alpha} = \mathscr{F}^{0} \tag{81}$$

So the image reconstructs when doing the FRFT with a correct order $-\alpha$. If we make the order α as a key, the encryption reforms only when inputting the correct key.

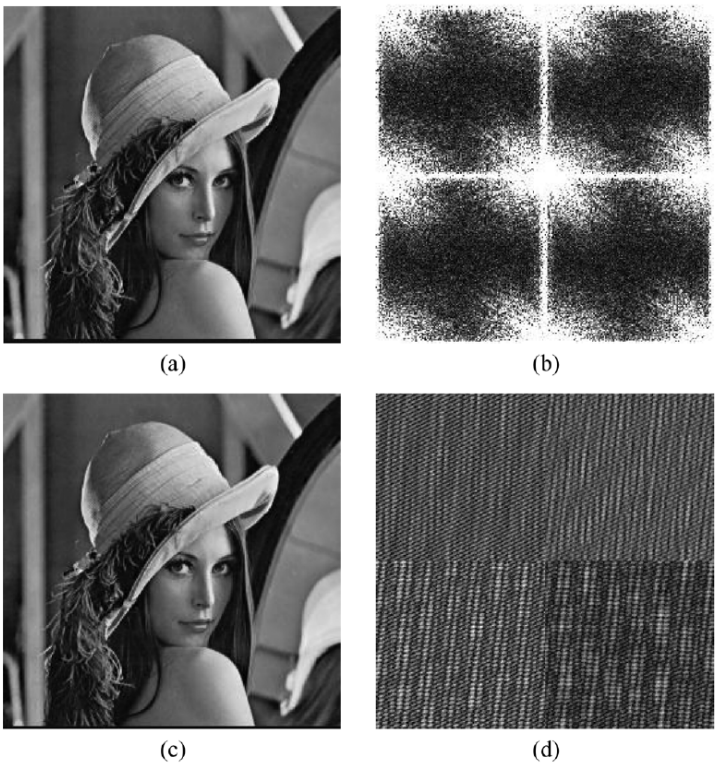

Figure 57: (a)Original image; (b)Encrypted image; (c)Correct decrypted image; (d)Decrepted image with incorrect transform orders

This method successfully encrypt the image, which only decrypt the image when receiving the correct key. However, this algorithm can be cracked through an optical experiment. The reconstructed image may eventually appear at a certain position. Thus, this simple encryption algorithm is weak on encrypting.

To encrypt the image, the FrTFL can replace the FRFT. The FRFT regenerate the image on a plane, but FrTFL can regenerate images in a complex surface. We can set the depth option as the key, generate the hologram of the image of the key, and decrypt with the same key. This bring a higher robustness to the encryption, because it is hard to crack the encryption with a certain surface through optical experiments.

A simple encryption algorithm was made for test. The depth limitation is changed, the origin image is "mandrill" and the depth is set as a irregular surface, as Fig. shows. The intensity and phase distribution of the diffraction is shown as Fig. .

When decrypting, if the key depth option is not correct, for example, a plane,

the decrypted image is totally incorrect. In the other hand, if the key depth option is correct, the image decrypts correctly as Fig. shows.

5.3 Image compression using FrTFL

There is an algorithm for depression using Fresnel transform, a kind of algorithm is to compress multiple images in a holograph, and regenerate images from different direction and different depth. However, the conventional method does not optimize the images in different positions simultaneously, which make the noise on other images while doing optimizations on a certain image.

A typical example is the algorithm as Fig. 58 shows.

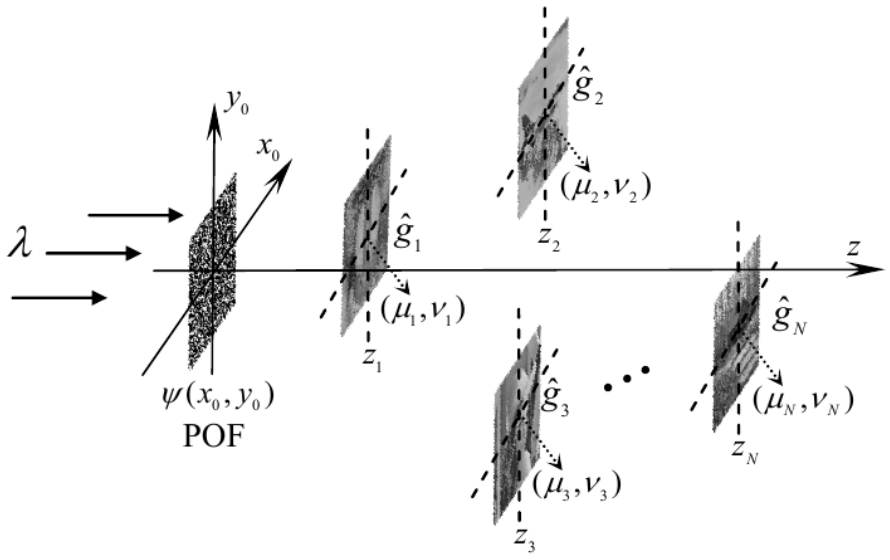

Figure 58: Holograph of multiple images at different positions

Thus, by adopting the FrTFL, this problem get solved perfectly. This compression algorithm is a lossy compression, which bring a noise on the original image.

A compression algorithm can be designed as following.

- Merge the images to a big image.
- Calculate the hologram of the new merged image.

5.4 Blind watermark using FrTFL

Blind watermark is a technology to add a watermark to images with a invisible method. Blind watermark are widely utilized in copyright and possesses legal validity. Artists use bind watermarks for anti-counterfeiting as well.

The simplest method to add watermark is to do the Fourier transform to the target image, and change the phase or amplitude value of the zone of high frequency, and then do the inverse Fourier transform to the modified image. This method highly hide the information into the image without changing the image too much.

The Fig. 59 and 60 shows an image and the image with a blind watermark. It is hard to see the difference between two images, however, invisible watermark is hided in the image.

Figure 59: Original image

Figure 60: Image with blind mark

The image without blind watermark does not have any information after doing Fourier transform. The image with blind watermark shows some information as Fig. 61.

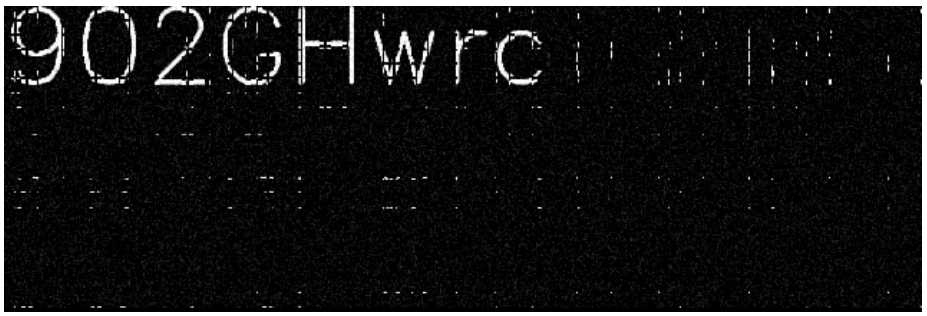

Figure 61: The blind watermark

Blind watermark hide information in the Fourier zone. It is very hard to find the watermark, however, if someone knows about such technology, the watermark may be disclosed.

Blind watermark is highly rely on the Fourier transform. Thus, the FrTFL may bring new features on the algorithm. By adding a depth key to the watermark, the watermark is encrypted that the hided information is encrypted. Without the depth key, the blind watermark would not be disclosed.

6 Conclusions

A Gradient-Descent based algorithm for phase-only CGH of 2D and 3D images was designed, which efficient is far better than the GS algorithm and modified GS algorithm.

For generating holograms of 3D images, a Fresnel transform with the utilization of a Fourier lens was developed. This tranform brings a new feature that able to regenerate 3D images with the utilization of Fourier lens.

A comparison of gradient-descent based optimization schemes was made to check the best optimization scheme on the phase-only CGH task. Adam tend to be the best algorithm for phase-only CGH calculating.

The FrTFL brings more possibilities on the fiesds of Fourier transform or Fractional Fourier transform. The FrTFL brings new feature on the task of image encryption, compression and blind watermark making.

Acknowledgement

This research is completed under the guidance of my supervisor, the Professor Takaki. My deepest gratitude goes first to Professor Takaki. Without his consistent instruction, the thesis would not reach the present form.

Second, my thanks would go to my coworker that assist my experiment, Master Takekawa. His assistance perfectly complete the experiment in the Section 2.

Then, my tanks would go to all members of the Lab Takaki. through 6 years. This is a great time in my life in this incredible Lab. As a forigner, I get helped much from members.

Last, I am indebted to parents for thier continuous supporting and encouraging.

References

[1] Dennis Gabor. A new microscopic principle. *nature*, 161:777–778, 1948.

[2] Dennis Gabor. Microscopy by reconstructed wave-fronts. *Proceedings of the Royal Society of London. Series A. Mathematical and Physical Sciences*, 197(1051):454–487, 1949.

[3] Stig Lundqvist. *Physics 1971-1980*, volume 1. World scientific, 1992.

[4] Rebecca Coyle. *Holography: art in space of technology*. Culture, technology and creativity in the late twentieth century, John Libbey/ Arts Council of Great Britain, 1990.

[5] Hideyoshi Horimai and Xiaodi Tan. Holographic versatile disc system. In *Organic Holographic Materials and Applications III*, volume 5939, page 593901. SPIE, 2005.

[6] Hideyoshi Horimai and Yoshio Aoki. Holographic versatile disc (hvd) system. In *2006 Optical Data Storage Topical Meeting*, pages 6–8. IEEE, 2006.

[7] Hideyoshi Horimai and Xiaodi Tan. Holographic information storage system: today and future. *IEEE Transactions on Magnetics*, 43(2):943–947, 2007.

[8] Hideyoshi Horimai and Xiaodi Tan. Read-only holographic versatile disc system using laser diode. In *Holography 2005: International Conference on Holography, Optical Recording, and Processing of Information*, volume 6252, page 62520Z. International Society for Optics and Photonics, 2006.

[9] Satyamoorthy Kabilan, Alexander J Marshall, Felicity K Sartain, Mei-Ching Lee, Abid Hussain, Xiaoping Yang, Jeff Blyth, Njeri Karangu, Karen James, Jimmy Zeng, et al. Holographic glucose sensors. *Biosensors and Bioelectronics*, 20(8):1602–1610, 2005.

[10] Alexander J Marshall, Jeff Blyth, Colin AB Davidson, and Christopher R Lowe. ph-sensitive holographic sensors. *Analytical Chemistry*, 75(17):4423–4431, 2003.

[11] Hyunmoon Nam, Kyungjun Song, Dogyeong Ha, and Taesung Kim. Inkjet printing based mono-layered photonic crystal patterning for anti-counterfeiting structural colors. *Scientific reports*, 6(1):1–9, 2016.

[12] Roxana Tomescu, Catalin Parvulescu, Dana Cristea, Brandus Comanescu, and Mihaela Pelteacu. Low cost technology for the fabrication of anti-counterfeiting microtaggants. *Journal of Micromechanics and Microengineering*, 31(3):035008, 2021.

[13] Nina V Markova, Leonid S Yamnikov, Elena S Turkina, Erick G Semenov, Theodor V Bulygin, and Gennady G Levin. Application of photopolymer holograms for the anticounterfeit protection of banknotes. In *Optical Security and Counterfeit Deterrence Techniques II*, volume 3314, pages 320–323. International Society for Optics and Photonics, 1998.

[14] Emily Sonnex, Matthew J Almond, John V Baum, and John W Bond. Identification of forged bank of england£ 20 banknotes using ir spectroscopy. *Spectrochimica Acta Part A: Molecular and Biomolecular Spectroscopy*, 118:1158–1163, 2014.

[15] MTHRGDM Campbell, DN Sharp, MT Harrison, RG Denning, and AJ Turberfield. Fabrication of photonic crystals for the visible spectrum by holographic lithography. *Nature*, 404(6773):53–56, 2000.

[16] Xia Wang, JF Xu, HM Su, ZH Zeng, YL Chen, HZ Wang, YK Pang, and WY Tam. Three-dimensional photonic crystals fabricated by visible light holographic lithography. *Applied Physics Letters*, 82(14):2212–2214, 2003.

[17] Jianghao Xiong, Kun Yin, Kun Li, and Shin-Tson Wu. Holographic optical elements for augmented reality: principles, present status, and future perspectives. *Advanced Photonics Research*, 2(1):2000049, 2021.

[18] Boaz Jessie Jackin, Lode Jorissen, Ryutaro Oi, Jui Yi Wu, Koki Wakunami, Makoto Okui, Yasuyuki Ichihashi, Philippe Bekaert, Yi Pai Huang, and Kenji Yamamoto. Digitally designed holographic optical element for light field displays. *Optics Letters*, 43(15):3738–3741, 2018.

[19] Boaz Jessie Jackin, Lode Jorissen, Ryutaro Oi, Koki Wakunami, Yasuyuki Ichihashi, Makoto Okui, Philippe Bekaert, and Kenji Yamamoto. Digitally designed hoe lens arrays for large size see-through head up displays. In *Frontiers in Optics*, pages FTh3E–2. Optical Society of America, 2018.

[20] R. W. Gerchberg and A Saxton W. O. A practical algorithm for the determination of phase from image and diffraction plane pictures. *Optik*, 35:237–250, 1972.

[21] Zeev Zalevsky, David Mendlovic, and Rainer G Dorsch. Gerchberg–saxton algorithm applied in the fractional fourier or the fresnel domain. *Optics Letters*, 21(12):842–844, 1996.

[22] Matthew Pasienski and Brian DeMarco. An algorithm for designing high-accuracy arbitrary holographic atom traps. In *Optical Trapping and Optical Micromanipulation V*, volume 7038, page 70381D. International Society for Optics and Photonics, 2008.

[23] Jared M Maxson, Adam C Bartnik, and Ivan V Bazarov. Efficient and accurate laser shaping with liquid crystal spatial light modulators. *Applied Physics Letters*, 105(17):171109, 2014.

[24] Andrew G Kirk and Trevor J Hall. Design of binary computer generated holograms by simulated annealing: coding density and reconstruction error. *Optics communications*, 94(6):491–496, 1992.

[25] Mengtao Wen, Jianping Yao, Wing Kee Wong, and George CK Chen. Holographic diffuser design using a modified genetic algorithm. *Optical Engineering*, 44(8):085801, 2005.

[26] Jun-Won An, Jae-Kwang Choi, Nam Kim, Seok-Hee Jeon, Young Soo Kwon, et al. Hybrid algorithm to reduce the computation time of genetic algorithm for designing binary phase holograms. *Optical Engineering*, 43(9):2061–2065, 2004.

[27] Jean-Numa Gillet and Yunlong Sheng. Multiplexed computer-generated holograms with polygonal-aperture layouts optimized by genetic algorithm. *Applied optics*, 42(20):4156–4165, 2003.

[28] Michael A Seldowitz, Jan P Allebach, and Donald W Sweeney. Synthesis of digital holograms by direct binary search. *Applied optics*, 26(14):2788–2798, 1987.

[29] Thibault Leportier, Min Chul Park, You Seok Kim, and Taegeun Kim. Converting optical scanning holograms of real objects to binary fourier holograms using an iterative direct binary search algorithm. *Optics Express*, 23(3):3403–3411, 2015.

[30] Thibault Leportier and Min-Chul Park. Advanced dbs (direct-binary search) method for compensating spatial chromatic errors on rgb digital holograms in a wide-depth range with binary holograms. *IEICE TRANSACTIONS on Fundamentals of Electronics, Communications and Computer Sciences*, 101(5):848–849, 2018.

[31] Shujian Liu and Yasuhiro Takaki. Optimization of phase-only computer-generated holograms based on the gradient descent method. *Applied Sciences*, 10(12):4283, 2020.

[32] Hone-Ene Hwang, Hsuan T Chang, and Wen-Nung Lie. Fast double-phase retrieval in fresnel domain using modified gerchberg-saxton algorithm for lensless optical security systems. *Optics express*, 17(16):13700–13710, 2009.

[33] James R Fienup. Phase retrieval algorithms: a comparison. *Applied optics*, 21(15):2758–2769, 1982.

[34] Shujian Liu and Yasuhiro Takaki. Gradient descent based algorithm of generating phase-only holograms of 3d images. *Optics Express*, 30(10):17416–17436, 2022.